Research Square

Preprints are preliminary reports that have not undergone peer review. They should not be considered conclusive, used to inform clinical practice, or referenced by the media as validated information.

Post-extinction recovery of the Phanerozoic oceans and the rise of biodiversity hotspots

Pedro Cermeño (pedrocermeno@icm.csic.es)
Instituto de Ciencias del Mar, CSIC https://orcid.org/0000-0002-3902-3475

Carmen García-Comas
Instituto de Ciencias del Mar, CSIC

Alexandre Pohl
University of California Riverside https://orcid.org/0000-0003-2328-351X

Simon Williams
Northwest University

Michael Benton
University of Bristol https://orcid.org/0000-0002-4323-1824

Guillaume Le Gland
Instituto de Ciencias del Mar, CSIC

R Dietmar Muller
The University of Sydney https://orcid.org/0000-0002-3334-5764

Andy Ridgwell
University of California, Riverside https://orcid.org/0000-0003-2333-0128

Sergio Vallina
Instituto Español de Oceanografía

Biological Sciences - Article

Keywords: biodiversity, diversity hotspots, Phanerozoic

Posted Date: October 28th, 2021

DOI: https://doi.org/10.21203/rs.3.rs-1013308/v1

License: This work is licensed under a Creative Commons Attribution 4.0 International License.
Read Full License

Version of Record: A version of this preprint was published at Nature on July 13th, 2022. See the published version at https://doi.org/10.1038/s41586-022-04932-6.

Post-extinction recovery of the Phanerozoic oceans and the rise of biodiversity hotspots

Pedro Cermeño[1,†,*], Carmen García-Comas[1,†], Alexandre Pohl[2,3], Simon Williams[4], Michael J. Benton[5], Guillaume Le Gland[1], R. Dietmar Müller[6], Andy Ridgwell[2], Sergio M. Vallina[7]

[1]*Institut de Ciències del Mar, Consejo Superior de Investigaciones Científicas, Pg. Marítim de la Barceloneta 37-49, 08003 Barcelona, Spain.*

[2]*Department of Earth and Planetary Sciences, University of California, Riverside, Riverside, CA, USA.*

[3]*Biogéosciences, UMR 6282, UBFC/CNRS, Université Bourgogne Franche-Comté, 6 boulevard Gabriel, F-21000 Dijon, France.*

[4]*State Key Laboratory of Continental Dynamics, Department of Geology, Northwest University, Xi'an, China.*

[5]*School of Earth Sciences, University of Bristol, Queens Road, Bristol, BS8 1RJ UK.*

[6]*EarthByte Group, School of Geosciences, University of Sydney, NSW, 2006, Sydney, Australia.*

[7]*Instituto Español de Oceanografía, Ave. Principe de Asturias 70 bis, 33212 Gijón, Spain.*

[†]*These authors contributed equally to this work*

**Corresponding author: pedrocermeno@icm.csic.es*

Abstract

The fossil record of marine invertebrates has long fueled the debate on whether or not there are limits to global diversity in the sea[1–4]. Ecological theory states that as diversity grows and ecological niches are filled, the strengthening of biological interactions imposes limits on diversity[5–7]. However, the extent to which biological interactions have constrained the growth of diversity over evolutionary time remains an open question[1–4,8–12], largely because of the incompleteness and spatial heterogeneity of the fossil record[13–15]. Here we present a regional diversification model that reproduces surprisingly well the Phanerozoic trends in the global diversity of marine invertebrates after imposing mass extinctions. We find that the dynamics of global diversity is best described by a diversification model that operates broadly within the exponential growth regime of a logistic function. A spatially resolved analysis of the diversity-to-carrying capacity ratio reveals that only < 2% of the global flooded continental area exhibits diversity levels approaching ecological saturation. We attribute the overall increase in global diversity during the Late Mesozoic and Cenozoic to the development of diversity hotspots under prolonged conditions of Earth system stability and maximum continental fragmentation. We call this the "diversity hotspots hypothesis", which is proposed as a non-mutually exclusive alternative to the hypothesis that the Mesozoic marine revolution led this macroevolutionary trend[16,17].

Main text

The question of whether or not there is an equilibrium diversity that the biota, or portions of the biota, cannot exceed has led to decades of debate between those who think that there is a limit to the global diversity that the Earth can carry[2,3,11,18] (i.e., a carrying capacity or saturation level) and those who think that diversity can increase in an unlimited fashion over time or, alternatively, that the biosphere is so far from the equilibrium diversity (i.e., its carrying capacity) that we can ignore the existence of any limit[8,9,12]. This question has traditionally been addressed by examining the shape of global fossil diversity curves[3,19]. For example, the Paleozoic plateau in marine invertebrate diversity is generally taken as strong evidence for the existence of ecological limits to further diversification[3,20]. However, because diversity varies dramatically among geographic regions, and each geographic region has its own geological and environmental history, addressing this question requires simultaneously reconstructing the dynamics of regional diversity in both space and time[14,21]. If diversity dynamics were governed by diversity-dependent feedbacks on speciation and extinction rates, then regional diversity should remain stable regardless of time once carrying capacity had been reached (i.e., the logistic model). The reasoning is the same as that used to explain the logistic growth model in population dynamics in which the per capita rate of increase decreases as the population approaches its maximum size or carrying capacity. Conversely, if evolutionary rates were independent of standing diversities, then we should observe positive relationships between evolutionary time-within-regions (or time-for-speciation) and diversity; the older the habitat the longer the lineages have had to diversify and fill empty niches or explore new ones (i.e., the exponential model). The reasoning in this case is the same as that used to explain the exponential growth model in population dynamics in which the per capita rate of increase does not depend on the population size but only on the modulating effects of environmental conditions. Determining which diversification model best

describes the dynamics of regional diversity over time is key to understanding the mechanisms underlying biogeographic patterns and macroevolutionary trends. However, the fossil record is biased by the inequality of the geographic and stratigraphic sampling effort[13,14], and the inequality in the rock record available for sampling[22], hindering our ability to investigate the effect of geographic variability in evolutionary time and diversification rate.

In order to overcome this limitation, we couple two alternative models of diversification, logistic and exponential, to a global plate motion model that constrains evolutionary time-within-regions (i.e. the age of the seafloor for the deep ocean and the time underwater for the flooded continental regions), Then, we reconstruct the spatial distributions and time trajectories of marine benthic animal divesity throughout the Phanerozoic. In both diversification models, the net diversification rate varies within a fixed range of values as a function of seawater temperature and food supply, which are reconstructed using a spatially-explicit Paleo-Earth system model (see Methods). The effects of temperature and food supply are parameterized, respectively, using a Q_{10} coefficient and a non-linear food limitation factor, under the premise that increasing temperature and food supply increase the rate of genus origination by shortening individuals' generation times and increasing population sizes, respectively. In the logistic model, the spatially resolved effective carrying capacities (K_{eff}) are allowed to vary within a fixed range of values (K_{min} and K_{max}) as a positive linear function of the food supply in each ocean region and time. That is, those regions with the lowest and highest food supply are assigned K_{min} and K_{max}, respectively, while those regions with intermediate levels of food supply are assigned K_{eff} values within the range K_{min} to K_{max}, accordingly. Finally, mass extinctions are imposed by imputing negative net diversification rates to regional communities and assuming non-selective extinction. The percentage of diversity loss as well as the starting time and duration of mass extinctions are extracted from three fossil diversity curves of reference, namely Sepkoski[23], Alroy[24] and Zaffos et al[25]. Each

of these curves provide alternative insights into the Phanerozoic history of marine animal diversity based on uncorrected range-through genus richness estimates[23,25] and sampling standardized estimates[24].

Seeking diversity hotspots in Phanerozoic oceans

There are clear differences in the spatial distributions of diversity generated by the logistic model and the exponential model as illustrated for 4 representative time-slices in the Phanerozoic (***Figure 1*** and ***Extended Data Figures 1 and 2***; see ***Supplementary Videos 1 and 2*** (***password****: video2021*) for the full Phanerozoic sequences). Regardless of the diversification model, most of the diversity is concentrated in shallow marine environments, where high temperatures and abundant food supplies increase the rates of diversification compared to deep-sea benthic habitats (***Fig. 1****,* ***Extended Data Fig. 1*** **and** ***2***). However, while regional diversity increases unconstrained in the exponential model, carrying capacities limit the growth of regional diversity in the logistic model, preventing the development of ocean regions with exceptionally high levels of diversity, hereinafter diversity hotspots.

Diversity hotspots occur in tropical shelf seas of the Early Devonian, Permian, Late Cretaceous and Cenozoic (***Fig. 1e-h***, ***Extended Data Fig. 1e-h and 2e-h***, and ***Supplementary Video 2***) (***password****: video2021*). During the early Devonian, diversity hotspots developed on the western continental margins of Laurentia and Siberia as well as on the tropical shelves of Gondwana. The recovery of Laurentian diversity hotspots after the Late Devonian mass extinction led to the onset of Permian hotspots, which eventually disappeared during the Permian-Triassic mass extinction. Diversity hotspots became particularly prominent during the Late Cretaceous and Cenozoic in the western basins of the Tethys Ocean, the Arabian Peninsula, the Atlantic Caribbean-East Pacific and the Indo-West

Pacific provinces (***Fig. 1g, h**, **Extended Data Fig. 1g, h and 2g, h***). This temporal trend in the prominence of diversity hotspots cannot be explained by a secular increase in the maximum lifetime of shelf seas, a proxy for the maximum potential evolutionary time-within-regions. Sedimentary data (i.e., magnetic anomalies in ancient continental margins trapped within orogenic belts)[26] and global tectonic reconstructions[27], including our reconstruction (***Supplementary Fig. 1***), show no evidence of an increase in the lifespan of passive continental margins or in the maximum ages of the seafloor over the Phanerozoic. Rather, we argue that the temporal proximity between the Ordovician-Silurian (Hirnantian), Late Devonian (Frasnian-Famennian), and Permian-Triassic mass extinctions, coinciding with a long-lived phase of continental coalescence and coastline destruction, interrupted the full development of diversity hotspots during the Paleozoic. By contrast, the comparatively long expanse of time that separated the mass extinctions of the end-Triassic and end-Cretaceous extended the time-for-speciation under conditions of increasing continental fragmentation, giving rise to exceptionally high diversity regions before the Cretaceous-Paleogene mass extinction. The extraordinary diversity of Late Cretaceous hotspots ensured the continuity of relatively high diversity levels in the aftermath of the end-Cretaceous mass extinction, facilitating the subsequent development of diversity hotspots during the Cenozoic.

Consistent with the patterns emerging from the fossil record of animal-like protists, such as large benthic foraminifera[28], the exponential model is able to reproduce the biogeography of diversity hotspots across the Late Cretaceous and Cenozoic (***Fig. 1g, h**, **Extended Data Fig. 1g, h and 2g, h**, and **Supplementary Video 2***) (***password**: video2021*). Our analysis suggests that these diversity hotspots were a consequence of the long residence time of shallow water seas within the tropical belt, leading to the establishment of three main tropical high diversity loci: the Paratethys-Mediterranean Sea, the Atlantic Caribbean-East Pacific, and the Indo-West Pacific. These spatial distribution patterns are remarkably consistent with

present-day geographical censuses of marine invertebrate diversity[29,30]. Our spatial reconstructions of diversity also confirm that the demise of Late Cretaceous and Paleogene diversity hotspots was largely driven by sea level fall and/or the deformation, either by subduction or uplift, of ancient chunks of the seafloor at continent-continent and arc-continent convergence zones, where the life cycle of ocean basins comes to an end (***Supplementary Video 2***).

Reconstructing global diversity dynamics

Each of the two diversification models tested here produces a total of 82 spatially-explicit reconstructions of diversity spanning from the Cambrian to the present. On each of the diversity distribution maps, we trace hundreds of line transects from diversity peaks to their nearest diversity troughs and integrate the total diversity in each transect by assuming a decay function in taxonomic similarity with geographic distance (see Material and Methods and ***Supplementary Fig. 2)***. Then, for each of the 82 time intervals, all integrated diversities along transects are re-integrated step-wise, from the transect with the greatest diversity to the transect with the lowest one, assuming the same distance-decay function applied to individual transects. The resulting global diversity estimates are plotted against the mid point value of the corresponding time interval to generate a synthetic global diversity curve. Both the logistic model and the exponential model produce relatively similar global diversity dynamics over time (***Fig. 2***, ***Extended Data Fig. 3***). This was to be expected since the global diversity curves produced by both models are equally influenced by long-term variations in the global area of tropical shallow shelf seas[31,32] (***Extended Data Fig. 4***), which harbour the vast majority of the diversity of marine benthic animals. However, while both models show similar diversity dynamics, the amplitude of global diversity variations differ markedly between models depending on whether or not regional-scale diversities self-limit their increase over

time. The exponential model gives rise to conspicuous increases in global diversity from the Cambrian to Late Ordovician, Silurian to Early Devonian, Carboniferous (Lower to Upper Pennsylvanian), Early to Late Cretaceous, and Paleocene to present. The Permian-Triassic mass extinction event lowered global diversity to Early Paleozoic levels, but later diversification led Late Cretaceous and Neogene faunas to exceed the Mid-Paleozoic global diversity peak. These trends emerge consistently regardless of the mass extinctions pattern imposed, be it Sepkoski[23], Alroy[24], or Zaffos et al.[25] (***Fig. 2a, b, c***, respectively). Nevertheless, it is worth noting how well the exponential model reproduces the 'uncorrected' Sepkoski fossil diversity curve. The logistic model also reproduces the initial increase in diversity, from the Cambrian to Upper Ordovician and from the Silurian to Early Devonian (***Fig. 2***). However, unlike the exponential model, in the logistic model this initial upward trend is followed by a convex diversity pattern interrupted by a modest increase during the Cretaceous, which rarely exceeds the mid-Paleozoic global diversity peak in our set of simulations (***Fig. 2***).

Our logistic model allows the spatially-resolved effective carrying capacities (K_{eff}) to vary within a fixed range of values (from K_{min} to K_{max}) as a positive linear function of food availability in each ocean region and time. All other things being equal, the higher the K_{min} and K_{max} values, the longer the evolutionary time required to reach diversity saturation. Consequently, the choice of K_{min} and K_{max} critically influences the extent to which regional biotas reach saturation. In order to calibrate the K_{min} and K_{max} parameters, we run simulations of pair-wise K_{min} and K_{max} combinations in a geometric sequence of base 2, from 2 to 256 genera, and test the effect of changing the K_{min} and K_{max} values on the concordance between the normalized diversities generated by the model and those estimated from the fossil record (***Fig. 3***). Unlike other correlation coefficients, the Lin's concordance correlation coefficient[33] (CCC) combines measures of both precision and accuracy to determine how far the observed (experimental or modelled) data deviate from the line of perfect concordance or

gold standard, that is, the 1:1 line. We focus the analysis on the time series data between the end of one mass extinction and the beginning of the next, that is, considering those time intervals dominated by rising diversity trajectories, which are influenced by the mode of regional diversification. The Lin's CCC increases with increasing K_{min} and K_{max} until reaching a plateau except for the mass extinction pattern of Sepkoski for which it continues to increase even at the highest K_{min} and K_{max} values (***Fig. 3***, ***Extended Data Fig. 5, 6, and 7***). These results are consistently replicated using alternative values for the parameters of the model that define the temperature- and food-dependence of the net diversification rate (***Fig. 3,*** grey lines in insets, ***Extended Data Table 1***).

High K_{min} and K_{max} values (and thus high K_{eff}), imply the need for longer evolutionary times and/or higher diversification rates to reach diversity saturation. Therefore, the results of the calibration analysis suggest that, in broad regions of the ocean, diversity could have been systematically far from saturation. In order to corroborate it, we re-run the logistic model using the average of all K_{min} and K_{max} combinations giving a CCC greater than 0.70, hereinafter referred to as 'calibrated' logistic model ***Supplementary Video 3***) (***password****: video2021*) and analyse the spatial and temporal variability of the diversity-to-carrying capacity (K_{eff}) ratio. This ratio represents a quantitative index of how far (ratios close to zero) or how close (ratios close to one) are the regional faunas from noticing the effect of diversity-dependent ecological factors. The diversity-to-K_{eff} ratio falls below 0.25 in most of the ocean and throughout the Phanerozoic (***Fig. 4a-l****,* ***Extended Data Fig. 8****,* ***Supplementary Video 4***) (***password****: video2021*), supporting the idea that the dynamics of regional diversity would have been operating systematically well below K_{eff}.

Finally, we calculate the diversity-to-K_{eff} ratio along the flooded continental regions using the combinations of K_{min} and K_{max} that resulted from simulations with different parameter values

(***Fig. 3,*** grey lines in insets, ***Extended Data Table 1***), and represent its frequency distributions (***Fig. 4m-o, Extended Data Fig. 8***). Most of the estimates fall within the exponential growth regime of the logistic function (i.e. diversity-to-K_{eff} ratio < 0.25). On average, less than 10% of the estimates exceed the threshold of 0.25, and only < 2% of the estimates, those associated with well-developed diversity hotspots, exceed the threshold of 0.5.

It is unlikely that our calibration analysis leads to an overestimation of K_{eff} since the CCC threshold of 0.7 imposed for the calculation of K_{min} and K_{max} would have led, if anything, to an understimation of K_{min} and K_{max} and thus, K_{eff}. Nonetheless, a deliberate decrease of 25% in the K_{min} and K_{max} values of the model does not alter significantly the shape of the diversity-to-K_{eff} ratio frequency distributions (***Extended Data Fig. 9***), which indicates that the resulting patterns are indeed robust. Furthermore, the paucity of diversity hotspots during the Paleozoic points to a scenario in which the relatively short time elapsed between successive mass extinctions interrupted their development. In fact, by deactivating the Late Devonian mass extinction in the model, we find that the full development of diversity hotspots before the end of the Permian leads to global diversities two to four times greater than those generated by the same 'calibrated' logistic model but with all mass extinctions enabled (***Extended Data Fig. 10***). We cannot reject the hypothesis that diversity saturation slowed down diversification processes in ocean regions where diversity hotspots i) had long development times, ii) evolved fast or iii) evolved from relatively high initial diversities (***Fig. 4***). Nevertheless, the slowdown and eventual halt of diversity growth at hotspots would not have prevented global diversity from continuing to grow as new diversity hotspots emerged elsewhere.

Discussion

We have shown that the development of biodiversity hotspots accounts for much of the increase in the global diversity of marine benthic animals throughout the Phanerozoic. Our analysis reveals that the temporal proximity between successive mass extinction events, along with the long-term reduction in the length of the coastline during the assembly of Pangea, interrupted the development of diversity hotspots during the Paleozoic. We find evidence of regional biota approaching diversity saturation at post-Paleozoic diversity hotspots, the development of which helps explain the increase in global diversity during the Late Mesozoic and Cenozoic. We call this the 'diversity hotspots hypothesis', which is proposed as an non-mutually exclusive alternative or supplement to the hypothesis that the Mesozoic marine revolution, that is, the evolutionary emergence of the durophagous predators and the ensuing cascade diversification, led this macroevolutionary trend[16,17].

With the possible exception of well-developed diversity hotspots, our results indicate that the diversity of marine benthic animals has remained well below saturation levels throughout their evolutionary history, shedding light on one of the most controversial questions in evolutionary ecology[2,3,8,9,11,12,18,34]. A taxonomic diversification model operating widely within the exponential growth regime of the logistic function implies a concave-upward relationship between the magnitude of diversity loss (x-axis) and the subsequent rebuilding time. This mode of diversification provides the most plausible explanation for the observed decoupling between mass extinctions and evolutionary radiations[35] over the Phanerozoic. We envision that our spatially-explicit reconstructions of diversity may shed light on other long-standing questions in (paleo)biogeography and macroevolution.

References

1. Raup, D. M. Species diversity in the Phanerozoic: An interpretation. *Paleobiology* **2**, 289–297 (1976).

2. Sepkoski, J. J. A kinetic model of Phanerozoic taxonomic diversity. III. Post-Paleozoic families and mass extinctions. *Paleobiology* **10**, 246–267 (1984).

3. Alroy, J. *et al.* Phanerozoic trends in the global diversity of marine invertebrates. *Science* **321**, 97–100 (2008).

4. Benton, M. J. The Red Queen and the Court Jester: Species diversity and the role of biotic and abiotic factors through time. *Science* **323**, 728-732 (2009).

5. MacArthur, R. H. & Wilson, E. O. *The Theory of Island Biogeography.* (Princeton University Press, 1967).

6. Simberloff, D. S. Equilibrium Theory of Island Biogeography and Ecology. *Annu. Rev. Ecol. Syst.* **5** (1974).

7. Warren, B. H. *et al.* Islands as model systems in ecology and evolution: Prospects fifty years after MacArthur-Wilson. *Ecology Letters* **18** (2015).

8. Stanley, S. M. An Analysis of the History of Marine Animal Diversity. *Paleobiology* **33**, 1–55 (2007).

9. Benton, M. J. & Emerson, B. C. How did life become so diverse? The dynamics of diversification according to the fossil record and molecular phylogenetics. in *Palaeontology* **50**, 23–40 (2007).

10. Bush, A. M., Bambach, R. K. & Daley, G. M. Changes in theoretical ecospace utilization in marine fossil assemblages between the mid-Paleozoic and late Cenozoic. *Paleobiology* **33**, 76–97 (2007).

11. Rabosky, D. L. & Hurlbert, A. H. Species richness at continental scales is dominated by ecological limits. *Am. Nat.* **185**, 572–583 (2015).

12. Harmon, L. J. & Harrison, S. Species diversity is dynamic and unbounded at local and continental scales. *Am. Nat.* **185**, 584–593 (2015).

13. Alroy, J. *et al.* Effects of sampling standardization on estimates of Phanerozoic marine diversification. *Proc. Natl. Acad. Sci. U. S. A.* **98**, 6261–6266 (2001).

14. Close, R. A., Benson, R. B. J., Saupe, E. E., Clapham, M. E. & Butler, R. J. The spatial structure of Phanerozoic marine animal diversity. *Science* **368**, 420–424 (2020).

15. Peters, S. E. Geologic constraints on the macroevolutionary history of marine animals. *Proc. Natl. Acad. Sci. U. S. A.* **102**, 12326–12331 (2005).

16. Vermeij, G. J. The mesozoic marine revolution: Evidence from snails, predators and grazers. *Paleobiology* **3**, 245–258 (1977).

17. Vermeij, G. J. *Evolution and Escalation*. *Evolution and Escalation* (Princeton University Press, 2021). doi:10.2307/j.ctv18zhf8b.

18. Simpson, G. G. *The Major Features of Evolution*. *The Major Features of Evolution* (Columbia University Press, 1953). doi:10.7312/simp93764.

19. Benton, M. J. Models for the diversification of life. *Trends in Ecology and Evolution* **12**, 490–495 (1997).

20. Sepkoski, J. J. A kinetic model of Phanerozoic taxonomic diversity II. Early Phanerozoic families and multiple equilibria. *Paleobiology* **5**, 222–251 (1979).

21. Vermeij, G. J. & Leighton, L. R. Does global diversity mean anything? *Paleobiology* **1**, 3–7 (2003).

22. Peters, S. E. & Foote, M. Determinants of extinction in the fossil record. *Nature* **416**, 420–424 (2002).

23. Sepkoski, J. J. J. A compendium of fossil marine animal genera. Edited by David Jablonski and Michael Foote. *Bull. Am. Paleontol.* **363**, 1–560 (2002).

24. Alroy, J. The shifting balance of diversity among major marine animal groups. *Science* **329**, 1191–1194 (2010).

25. Zaffos, A., Finnegan, S. & Peters, S. E. Plate tectonic regulation of global marine animal diversity. *Proc. Natl. Acad. Sci. U. S. A.* **114**, 5653–5658 (2017).

26. Bradley, D. C. Passive margins through earth history. *Earth-Science Reviews* **91**, 1–26 (2008).

27. Müller, R. D. *et al.* Ocean Basin Evolution and Global-Scale Plate Reorganization Events since Pangea Breakup. *Annual Review of Earth and Planetary Sciences* **44**, 107–138 (2016).

28. Renema, W. *et al.* Hopping hotspots: Global shifts in marine biodiversity. *Science* **321**, 654–657 (2008).

29. Edgar, G. J. *et al.* Abundance and local-scale processes contribute to multi-phyla gradients in global marine diversity. *Sci. Adv.* **3** (2017).

30. Costello, M. J. & Chaudhary, C. Marine Biodiversity, Biogeography, Deep-Sea Gradients, and Conservation. *Current Biology* **27** (2017).

31. Cao, W. *et al.* Improving global paleogeography since the late Paleozoic using paleobiology. *Biogeosciences* **14**, 5425–5439 (2017).

32. Kocsis, Á. T. & Scotese, C. R. Mapping paleocoastlines and continental flooding during the Phanerozoic. *Earth-Science Reviews* **213**, 103463 (2021).

33. Lin, L. I.-K. A Concordance Correlation Coefficient to Evaluate Reproducibility. *Biometrics* **45**, 255 (1989).

34. Erwin, D. H. Macroevolution of ecosystem engineering, niche construction and diversity. *Trends Ecol. Evol.* **23**, 304–310 (2008).

35. Hoyal Cuthill, J. F., Guttenberg, N. & Budd, G. E. Impacts of speciation and extinction measured by an evolutionary decay clock. *Nature* **588**, (2020).

Methods

Paleogeographic model

We derived paleogeographic reconstructions describing Earth's paleotopography and paleobathymetry for a series of time slices from 541 Ma to present day. The reconstructions merge existing models from two published global reconstruction datasets, those of Merdith et al[36] and Scotese and Wright[37] (https://doi.org/10.5281/zenodo.5348492), which themselves are syntheses of a wealth of previous work.

For continental regions, estimates of paleoelevation and continental flooding rely on a diverse range of geological evidence defining the past locations of mountain ranges and paleoshorelines[38]. For this part of our reconstruction, we used the compilation of Scotese and Wright[37] with updated paleoshorelines[32]. This compilation comprises 82 paleotopography maps covering the entire Phanerozoic. For deep ocean regions, the primary control on seafloor depth is the age of the seafloor, so reconstructing paleobathymetry relies on constructing maps of seafloor age back in time[39]. Consequently, we rely on reconstruction models that incorporate a continuous network of plate boundaries that allow us to derive maps of seafloor age in deep time. For this part, we used the reconstruction of Merdith et al[36] and derived maps of seafloor age from the plate tectonic model using the method of Williams et al[40], for which source code is available at https://github.com/siwill22/agegrid-0.1. Paleobathymetry was derived from the seafloor age maps following the steps outlined by Müller et al[39]. It is important to note that seafloor age maps for most of the Phanerozoic (i.e. pre-Pangea times) are not directly constrained by data due to recycling of oceanic crust at subduction zones. Rather, they are model predictions generated by constructing plate motions and plate boundary configurations from the geological and paleomagnetic record of

the continents. Nonetheless, the first order trends in ocean-basin volume and mean seafloor age are consistent with independent estimates for at least the last 410 Myr[40].

The reconstructions of Merdith et al[36] and Scotese and Wright[37] differ in the precise locations of the continents through time. To resolve this discrepancy, we reverse reconstructed the Scotese and Wright[37] continental paleoelevation model to present-day coordinates using their rotation parameters, then reconstructed them back in time using the rotations of Merdith et al[36]. Due to the differences in how the continents are divided into different tectonic units, this process leads to some gaps and overlaps in the results[31], which we resolved primarily through a combination of data interpolation and averaging. Manual adjustments were made to ensure that the flooding history remained consistent with the original paleotopography in areas where interpolation gave a noticeably different history of seafloor ages. The resulting paleotopography maps are thus defined in paleomagnetic reference frame[36] appropriate for use in Earth System models.

For the biodiversity modelling, we generate estimates of the age of the seafloor for discrete points within the oceans and flooded continents, and track these ages through the lifetime of each point. For the oceans, this is achieved using the method described by Williams et al[40] where the seafloor is represented by points incrementally generated at the mid-ocean ridges for a series of time-step 1 Myr apart, with each point tracked through subsequent time-steps based on Euler poles of rotation until either present-day is reached, or they arrive at a subduction zone and are considered destroyed.

For the continents, tracking the location of discrete points is generally simpler since most crust is conserved throughout the timespan of the reconstruction. Unlike the deep oceans (where we assume that crust is at all times submerged), we model the ‘age’ of the seafloor

from the history of continental flooding and emergence within the paleogeographic interpretation[37]. The continents are seeded with uniformly distributed points at the oldest timeslice (541 Ma) where they are assigned an age of zero. These points are tracked to subsequent time slices where the paleogeography is used to determine whether the point lies within a flooded or emergent region. Points within flooded regions of continents are considered to be seafloor, and the age of this seafloor is accumulated across consecutive time slices where a given point lies within a flooded region. When a point is within an emergent region, the seafloor age is reset to zero. Following this approach, individual points within stable continents may undergo several cycles of seafloor age increasing from zero before being reset. At the continental margins formed during Pangea breakup, the age of the seafloor continuously grows from the onset of rifting. Intra-oceanic island arcs represent an additional case, which can appear as new tectonic units with the reconstructions at various times. In these cases, we assume that the seafloor has a zero-age at the time the intra-oceanic arc first develops, then remains predominantly underwater for the rest of its lifetime. ***Supplementary figure 1a-d*** shows the estimated age of the seafloor for open ocean and flooded continental shelves using the approach described in this section.

Therefore, for each of the 82 paleogeographic reconstructions, we annotate 0.5º by 0.5º grids as continental, flooded continental shelf, or oceanic for later use in model coupling and production of regional diversity maps.

Paleo-environmental conditions: cGenie Earth System model

We use cGENIE[41], an Earth System model of intermediate complexity, to simulate paleo-environmental conditions, primarily seawater temperature and organic carbon export

production (as a surrogate for food supply) throughout the Phanerozoic (from 541 Ma to present day).

cGENIE is based on a 3-dimensional (3D) ocean circulation model coupled to a 2D energy-moisture-balance atmospheric component and a sea-ice module. We configured the model on a 36×36 (lat, lon) equal area grid with 17 unevenly spaced vertical levels in depth, down to a depth of 5,900 m. The cycling of carbon and associated tracers in the ocean is based on a single (phosphate) nutrient limitation of biological productivity accounting for plankton ecology[42,43], and adopts the Arrhenius-type temperature-dependent scheme for the remineralization of organic matter exported to the ocean interior[44].

cGENIE offers a spatially resolved representation of ocean physics and biogeochemistry, which is a prerequisite for the present study to be able of reconstructing the spatial patterns of biodiversity in deep time. Due to the ensuing computational cost, cGENIE cannot be used to generate transient simulations covering the entire last 541 Myr. In order to simulate ocean physics (i.e., temperature) and biogeochemistry (i.e., export production) during the Phanerozoic, we therefore generate (30) model equilibria at regular time intervals throughout the Phanerozoic. These Earth system model snapshots are subsequently used as inputs for the regional diversification model (see the Methods section Model coupling). Below, we describe the protocol adopted to generate each of those 30 model snapshots.

We use 30 Phanerozoic paleogeographic reconstructions through time (~20 Myr evenly spaced time intervals) produced by the plate tectonic/paleo-elevation model to represent key time periods. For each continental configuration corresponding to a given Earth's age, we generate idealized 2D wind speed and wind stress, and 1D zonally-averaged albedo forcing fields[45] required by the cGENIE model using the 'muffingen' open-source software (see code

availability section below). For each paleogeographic reconstruction, the climatic forcing (i.e., solar irradiance and carbon dioxide concentration) is adapted to match the corresponding geological time interval. The pCO_2 is taken from the recent update of the GEOCARB model[46]. Solar luminosity is calculated using the model of stellar physics of Gough[47]. We impose modern-day orbital parameters (obliquity, eccentricity and precession). The simulations are initialized with a sea-ice free ocean, homogeneous oceanic temperature (5 °C), salinity (34.9 ‰) and phosphate concentration (2.159 μmol kg^{-1}). Because variations in the oceanic concentration of bio-available phosphate remain challenging to reconstruct in the geological past[48,49], we impose a present-day mean ocean phosphate concentration in our baseline simulations. We quantify the impact of this uncertainty on our model results by conducting additional simulations using half and twice the present-day ocean phosphate concentration (***Extended Data Fig. 3***). For each ocean phosphate scenario (i.e., 0.5×, 1× and 2× the present-day value), each of the 30 model simulations is then integrated for 20,000 years, a duration ensuring that deep-ocean temperature and geochemistry reach equilibrium. For each model simulation, results of the mean annual values of the last simulated year are used for the analysis.

Regional diversification model

We test two models of diversification, the logistic model and the exponential model, describing the dynamics of regional diversity over time. In both models, the net diversification rate (ρ), with units of inverse time (Myr^{-1}), is the difference between the rates of origination and extinction and varies within a pre-fixed range of values as a function of seawater temperature and food availability. The implicit mechanism is that high temperatures and abundant food supplies increase the genus origination rates by shortening individual's generation times (i.e. higher metabolic rates) and increasing population sizes (i.e. higher

mutation probabilities), respectively. The net diversification rate is then calculated for a given location and time according to the following equation:

$$\rho = \rho_{max} - (\rho_{max} - \rho_{min})(1 - Q_{temp} Q_{food}) \qquad \textit{Equation 1}$$

where ρ_{min} and ρ_{max} set the lower and upper net diversification rate limits within which ρ is allowed to vary, and Q_{temp} and Q_{food} are non-dimensional limitation terms with values between 0 and 1 that define the dependence of ρ on temperature and food, respectively (see ***Supplementary Table 1***). These temperature and food supply limitation terms vary in space and time as a result of changes in seawater temperature and particulate organic carbon export rate, respectively, thereby controlling the spatial and temporal variability of ρ.

The temperature-dependence of ρ is calculated using the following equation:

$$Q_{temp} = \frac{Q_{10}^{\frac{T - Tmin}{10}}}{Q_{10}^{\frac{Tmax - Tmin}{10}}} \qquad \textit{Equation 2}$$

where the Q_{10} coefficient measures the temperature sensitivity of the origination rate. Assuming a constant background extinction rate, a Q_{10} coefficient of 2 would correspond to a doubling of the net diversification rate for every 10 ºC increase in temperature. In the equation 2 above, T is the seawater temperature (in ºC) at a given location and time, while T_{min} and T_{max} are the 0.01 percentile and the 0.99 percentile, respectively, of the temperature frequency distribution in each time interval. In the model, the values of T_{min} and T_{max} used to calculate Q_{temp} are thus recomputed every time interval (~ 5 Myr) according to the temperature frequency distribution of the corresponding time interval. This allows having

updated T_{min} and T_{max} in each Phanerozoic time interval and account for the thermal adaptation of organisms to ever-changing climate conditions.

The food limitation term is parameterized using a Michaelis-Menten formulation as follows:

$$Q_{food} = \frac{POC\,flux}{(K_{food} + POC\,flux)} \qquad \textit{Equation 3}$$

where *POC flux* (mol m^{-2} $year^{-1}$) is the particulate organic carbon export flux, which is used as a surrogate for food availability, at a given location and time of the simulated seafloor. The parameter K_{food} (mol m^{-2} $year^{-1}$) in equation 3 is the half-saturation constant, that is, the *POC flux* at which the diversification rate is half its maximum value, provided that other factors were not limiting. ***Supplementary figure 3*** shows the interactive effect of temperature and food supply on net diversification rate for the Q_{10} and K_{food} coefficients used to run the main simulations presented in ***Figure 1*** (i.e. Q_{10} = 1.75, K_{food} = 0.5 mol C $m^{-2}y^{-1}$) and two extreme parameter settings (i.e. Q_{10} = 1.5 and 2.5, K_{food} = 0.25 and 1 mol C $m^{-2}y^{-1}$). ***Supplementary figure 1e-h*** shows the spatial variability of the net diversification rate at four different times of the Phanerozoic.

Our modelling approach assumes a constant background extinction rate so that changes in net diversification rate (ρ) are implicitly governed by spatial and temporal variations in origination rates. Nonetheless, ρ becomes negative i) in the event of mass extinctions or ii) in response to regional-scale processes, such as sea-level fall and seafloor deformation along convergent plate boundaries. Mass extinction events are imposed as external perturbations to the diversification model by imputing negative diversification rates to all active seafloor points (ocean points and flooded continental points), and assuming non-selective extinction. The percentage of diversity loss as well as the starting time and duration of mass extinctions

are extracted from three fossil diversity curves of reference, namely Sepkoski[23], Alroy[24] and Zaffos et al[25] (***Supplementary Fig. 4***). Each of these fossil diversity curves provides different insights into the Phanerozoic history of marine animal diversity based on uncorrected range-through genus richness estimates[23,25] and sampling standardized estimates[24]. Regional-scale processes, such as sea level fall during marine regressions and/or seafloor destruction at plate boundaries (either by subduction or uplift), are simulated by the combined plate tectonic/paleo-elevation model, and constrain the time span that seafloor habitats have to accumulate diversity.

Letting *D* represent regional diversity (number of genera within a given seafloor point) and *t* represent time, the logistic model is formalized by the following differential equation:

$$\frac{\partial D(t)}{\partial t} = \rho D[1 - \frac{D}{K_{eff}}] \qquad \textit{Equation 4}$$

where $D(t)$ is the number of genera at time t and K_{eff} is the effective carrying capacity or maximum number of genera that a given seafloor point (i.e., grid cell area after gridding) can carry at that time, t. In our logistic model, K_{eff} is allowed to vary within a fixed range of values (from K_{min} to K_{max}) as a positive linear function of the *POC flux* at a given location and time as follows:

$$K_{eff} = K_{max} - (K_{max} - K_{min}) \frac{POC\,flux_{max} - POC\,flux}{POC\,flux_{max} - POC\,flux_{min}} \qquad \textit{Equation 5}$$

where $POC\ flux_{min}$ and $POC\ flux_{max}$ corresponds to the 0.01 and 0.99 quantiles of the *POC flux* range in the whole Phanerozoic dataset.

In the logistic model, the net diversification rate decreases as regional diversity approaches its K_{eff}. The exponential model is a particular case of the logistic model when K_{eff} approaches infinity and, therefore, neither the origination rate nor the extinction rate depend on the standing diversities. In this scenario, diversity grows in an unlimited fashion over time only truncated by externally imposed mass extinctions and/or by the dynamics of the seafloor (creation versus destruction). The exponential model is thus as follows:

$$\frac{\partial D(t)}{\partial t} = \rho D \qquad \textit{Equation 6}$$

where the rate of change of diversity (the time derivative) is proportional to the standing diversity D such that the regional diversity will follow an exponential increase in time at a speed controlled by the temperature- and food-dependent net diversification rate. Even if analytical solutions exist for the steady-state equilibrium of the logistic and exponential functions, we solved the ordinary differential equations (4) and (6) using numerical methods with a time lag of 1 Myr to account for the spatially- and temporally-varying environmental constraints, seafloor dynamics, and mass extinction events.

Because the analysis of global fossil diversity curves is unable to discern the causes of diversity loss during mass extinctions, our imputation of negative diversification rates could have overestimated diversity loss in those cases in which sea level fall, a factor already accounted for by our coupled diversification-plate tectonic model, contributed to mass extinction events. This effect was particularly recognizable across the Permo-Triassic mass extinction (***Extended Data Fig. 10***), and supports previous suggestions that the decline in global area of the shallow water shelf exacerbated the severity of the end-Permian mass extinction[38].

Model coupling

As stated above, the coupled plate tectonic/paleo-elevation (paleogeographic) model corresponds to a tracer-based model (a Lagrangian-based approach) that simulates and tracks the spatio-temporal dynamics of ocean and flooded continental points. The diversification models start at time 541 million years ago (Ma) with all active points having a D_0 = 1 (one single genus everywhere) and we let points to accumulate diversity heterogeneously with time according to seafloor age distributions (for ocean points) and the time that continents have been underwater (for flooded continental points). The ocean points are created at mid-ocean ridges and disappear primarily at subduction zones. In between their origin and demise, the points move following plate tectonic motions and we trace their positions while accumulating diversity. The flooded continental points begin to accumulate diversity from the moment they are submerged starting with a D value equal to the nearest neighbour flooded continental point with $D > 1$, thereby simulating a process of coastal re-colonization (or immigration). The diversification process remains active while the seafloor points remain underwater, but it is interrupted, and D set to 0, in those continental points that emerge above sea level. Likewise, seafloor points corresponding to ocean domains disappear in subduction zones, and their diversity is lost. We track the geographic position of the ocean and flooded continental points approximately every 5 Myr, from 541 Ma to the present. Each and every one of the tracked points accumulate diversity over time at a different rate, which is modulated by the environmental history (seawater temperature and food availability) of each point, as described in equations 1-3. When a point arrives to an environment with a carrying capacity lower than the diversity it has accumulated through time, we reset the diversity of the point to the value of carrying capacity, thereby simulating local extinction.

Seawater temperature (*T*) and food availability (*POC flux*) are provided by the cGENIE model, which has a spatial and temporal resolution coarser than the paleogeographic model. The cGENIE model provides average seawater *T* and *POC flux* values in a 36×36 equal area grid (grid cell area equivalent to 2º latitude by 10º longitude at the equator) and 30 time slices or snapshots (from 541 Ma to present: each ~20 Myr time intervals). To have environmental inputs for the 82 time slices of the plate tectonic/paleo-elevation model, we first interpolate the cGENIE original model output data on a 0.5º by 0.5º grid to match the annotated grids provided by the plate tectonic/paleo-elevation model. Because the relatively coarse spatial resolution of the cGENIE model prevents rendering the coast-ocean gradients, we assign surface *T* and *POC flux* at the base of the euphotic zone to the flooded continental shelf grid cells, and deep ocean *T* and *POC flux* at the bottom to the ocean grid cells. Because there are time slices without input data of seawater *T* and *POC flux*, we inter/extrapolate seawater *T* and *POC flux* values into the 0.5º by 0.5º flooded continental shelf and ocean grids independently. Finally, we interpolate values from these 0.5º by 0.5º flooded continental shelf and ocean grids into the exact point locations in each time frame. Therefore, each active point is tracked with its associated time-varying *T* and *POC flux* values throughout its lifetime. On average, 6,000 flooded continental points and 44,000 oceanic points were actively accumulating diversity in each time frame.

Estimation of global diversity from regional diversity

Our regional diversity maps are generated by separately interpolating ocean point diversity and flooded continental point diversity into the 0.5º by 0.5º annotated grids provided by the paleogeographic model. We calculate global diversity at each time step from each of the regional diversity maps following a series of steps to integrate diversity along line transects from diversity peaks (maxima) to diversity troughs (minima) (***Supplementary Fig. 2***). To

select the transects, first, we identify on each of the regional diversity maps the geographic position of the diversity peaks. The peaks are defined as the grid cells identified as local maxima (i.e., with diversity greater than their neighbour cells). In the case of grid cells with equal neighbour diversity, the peak is assigned to the grid cell in the middle point of the grids with equal diversity. We subsequently identify the geographic position of the diversity troughs, which are defined as newly formed ocean grid cells (age = 0 Myr) and, therefore, with diversities equal to one. The troughs are mostly located at mid-ocean ridges.

On each of the 82 spatial diversity maps, we trace a line transect from each diversity peak to its closest trough, provided that the transect does not cross land in more than 20 % of the grid cells along the linear path. On average, for each spatial diversity map, we trace 400 ($\sigma = \pm 75$) linear transects. This sampling design gives rise to transects of different lengths, which may bias the estimates of global diversity. To minimize this bias, we cut the tail of the transects to have a length of 555 km equivalent to 5º at the equator. We test an alternative cutoff threshold; 1110 km, and the results do not alter the study's conclusions.

We apply Bresenham's line algorithm[50] to detect the grid cells crossed by the transects and annotate their diversity. To integrate regional diversity along the transects, we develop a method to simplify the scenario of peaks and troughs heterogeneously distributed in the 2D diversity maps. The method requires i) a vector (the transect) of genus richness (α_n) at n different locations (grids) arranged in a line (1D) of L grids, and ii) a coefficient of similarity ($V_{n,n+1}$) between each two neighbouring locations, n and $n+1$. $V_{n,n+1}$, the coefficient of similarity, follows a decreasing exponential function with distance between locations. The number of shared genera between n and $n+1$ is $V_{n,n+1} * min(\alpha_n; \alpha_{n+1})$. We integrate diversity from peaks to troughs and assume that, along the transect, α_{n+1} is lower than α_n. We further

assume that the genera present in *n* and *n+2* cannot be absent from *n+1*. Using this method, we integrate the transect's diversity (γ_i) using the following equation:

$$\gamma_i = \alpha_1 + \sum_{n=1}^{L-1} (1 - V_{n,n+1}) \alpha_{n+1} \qquad \textit{Equation 7}$$

To integrate the diversity of all transects (γ_i) on each 2D diversity map (or time slice), we apply the same procedure as described above (***Supplementary Fig. 2***). We first sort the transects in descending order from the highest to the lowest diversity. Then, we assume that the number of shared genera between transect *i* and the rest of transects with greater diversity {1, 2,…, *i* -1} is given by the distance of its peak to the nearest neighbour peak [*NN*(i)] of those already integrated {1,2,… *i* -1}. Thus, we perform a zigzag integration of transects' diversities down gradient, from the greatest to the poorest, weighted by the nearest neighbour distance among the peaks already integrated. As a result, the contribution of each transect to global diversity will depend on its diversity and its distance to the closest transect from all those transects already integrated. With this method, we linearize the problem to simplify the cumbersome procedure of passing from a 2D regional diversity map to a global diversity estimate without knowing the identity (taxonomic affiliation) of the genera. Being γ_{total} the global diversity at time *t*:

$$\gamma_{total} = \gamma_1 + \sum_{i=2}^{i} (1 - V_{NN(i),i}) \gamma_i \qquad \textit{Equation 8}$$

Finally, the resulting global estimates are plotted against the mid point value of the corresponding time interval to generate a synthetic global diversity curve. In order to compare the global diversity curves produced by the diversification models with those composed from the fossil record, the Lin's concordance correlation coefficient (CCC)[33] is applied on the data

normalized to the min-max values of each time series (i.e., rescaled within the range 0-1). Lin's CCC combines measures of both precision and accuracy to determine how far the observed data deviate from the line of perfect concordance or gold standard (that is, the 1:1 line). Lin's CCC increases in value as a function of the nearness of the data's reduced major axis to the line of perfect concordance (the accuracy of the data) and of the tightness of the data around its reduced major axis (the precision of the data).

Model parameterization and calibration

The diversification models are parameterized assuming a range of values that constrain the lower and upper limit of the genus-level net diversification rate (ρ_{min} and ρ_{max}, respectively) (***Supplementary Table 1***) according to previously reported estimates from fossil records (Figures 8 and 11 of Stanley[8]). A range of realistic values is assigned for the parameters Q_{10} and K_{food} (***Supplementary Table 1***), determining, respectively, the thermal sensitivity and food dependence of the net diversification rate. We test a total of 40 different combinations of parameter settings (***Extended Data Table 1***). The resulting estimates of diversity are then compared against the fossil diversity curves of Sepkoski[23], Alroy[24], or Zaffos et al.[25], and the fifteen parameter settings providing the highest CCCs are selected.

The results of the logistic diversification model rely on the values of the minimum and maximum carrying capacities (K_{min} and K_{max}, respectively) within which the spatially-resolved effective carrying capacities (K_{eff}) are allowed to vary. The values of K_{min} and K_{max} are thus calibrated by running 28 simulations of pair-wise K_{min} and K_{max} combinations increasing in a geometric sequence of base 2, from 2 to 256 genera (***Figure 3***, ***Extended Data Fig. 5, 6, and 7***). We perform these simulations independently for each of the fifteen parameter

settings selected previously (***Extended Data Fig. 1***). Each combination of K_{min} and K_{max} produces a global diversity curve, which is evaluated as described above using Lin's CCC.

Calculating estimates of global diversity from regional diversity maps in the absence of information on genus-level taxonomic identities requires assuming a spatial turnover of taxa with geographic distance (***Supplementary Fig. 2***). Distance–decay curves are routinely fitted by calculating the ecological similarity (e.g. Jaccard similarity index) between each pair of sampling sites, and fitting an exponential decay function to the points on a scatter plot of similarity (y-axis) versus distance (x-axis). Following this method, we fit an exponential decay function to the distance-decay curves reported in Miller et al[51], depicting the decrease in the Jaccard similarity index (*J*) with geographic distance (great circle distance) at different Phanerozoic time intervals:

$$J = J_{off} + (J_{max} - J_{off})\, e^{\lambda * distance} \qquad \textit{Equation 9}$$

where J_{off} = 0.06 (n.d.) is a small offset, J_{max} = 1.0 (n.d.) is the maximum value of the genus-based Jaccard similarity index, and λ= 0.0024 (Km^{-1}) is the distance-decay rate.

The Jaccard similarity index *(J*) between consecutive points *n* and *n*+1 is bounded between 0 and $min(\alpha_n; \alpha_{n+1})/max(\alpha_n; \alpha_{n+1})$. A larger value for *J* would mean that there are more shared genera between the two communities than there are genera within the least diverse community, which is ecologically absurd. However, using a single similarity decay function can lead the computed value of *J* to be locally larger than $min(\alpha_n; \alpha_{n+1})/max(\alpha_n; \alpha_{n+1})$. To prevent this artifact, we use the Simpson similarity index or “overlap coefficient” (*V*) instead of *J*. *V* corresponds to the percentage of shared genera with respect to the least diverse community ($min(\alpha_n; \alpha_{n+1})$). *V* is bounded between 0 and 1, whatever the ratio of diversities.

As the pre-existing estimates of similarity are expressed using J[51], we make the conversion from J to V using the algebraic expression $V = (1 + R) * J / (1 + J)$ where $R = max(\alpha_n; \alpha_{n+1})/min(\alpha_n; \alpha_{n+1})$ (see ***Annex 1***). In the cases in which J exceeds the $min(\alpha_n; \alpha_{n+1})/max(\alpha_n; \alpha_{n+1})$, V becomes > 1 and, in those cases, we force V to be <1 by assuming $R = 1$, that is $\alpha_n = \alpha_{n+1}$.

Fossil data

We digitized three fossil diversity curves of reference, namely, Sepkoski[23], as depicted in figure 1b in Stanley[8], figure 3 in Alroy[24], and figure 2a in Zaffos et al[25]. The Sepkoski[23] and Zaffos et al[26] curves have no standardization by sampling effort; the first curve corresponds to well preserved marine invertebrate animals and protist groups listed in the Appendix of Sepkoski[23] and with intervals averaging 5.4 Myr; and the later corresponds to 1 Myr range-through richness of skeletonized marine animal genera. The fossil global diversity curve reported in the Alroy's study[24] was built using genus-richness estimates obtained after correcting for sampling effort using the shareholder quorum subsampling (SQS) technique. This curve is binned at approximately 11-Myr time intervals. All digitized (and interpolated) diversity data are provided as a source data file.

Additional references

36. Merdith, A. S. *et al.* Extending full-plate tectonic models into deep time: Linking the Neoproterozoic and the Phanerozoic. *Earth-Science Reviews* **214** (2021).

37. Scotese, C. R. & Wright, N. PALEOMAP Paleodigital Elevation Models (PaleoDEMS) for the Phanerozoic PALEOMAP Project, https://www.earthbyte.org/paleodem-resource-scotese-and-wright-2018/. (2018).

38. Scotese, C. R. An atlas of phanerozoic paleogeographic maps: The seas come in and the seas go out. *Annual Review of Earth and Planetary Sciences* **49**, 679–728 (2021).

39. Müller, R. D., Sdrolias, M., Gaina, C., Steinberger, B. & Heine, C. Long-term sea-level fluctuations driven by ocean basin dynamics. *Science* **319**, 1357–1362 (2008).

40. Williams, S., Wright, N. M., Cannon, J., Flament, N. & Müller, R. D. Reconstructing seafloor age distributions in lost ocean basins. *Geosci. Front.* **12**, 769–780 (2021).

41. Ridgwell, A. *et al.* Marine geochemical data assimilation in an efficient Earth system model of global biogeochemical cycling. *Biogeosciences* **4**, 87–104 (2007).

42. Ward, B. A. *et al.* EcoGEnIE 1.0: Plankton ecology in the cGEnIE Earth system model. *Geosci. Model Dev.* **11**, 4241–4267 (2018).

43. Wilson, J. D., Monteiro, F. M., Schmidt, D. N., Ward, B. A. & Ridgwell, A. Linking Marine Plankton Ecosystems and Climate: A New Modeling Approach to the Warm Early Eocene Climate. *Paleoceanogr. Paleoclimatology* **33**, 1439–1452 (2018).

44. Crichton, K. A., Wilson, J. D., Ridgwell, A. & Pearson, P. N. P. N. Calibration of temperature-dependent ocean microbial processes in the cGENIE.muffin (v0.9.13) Earth system model. *Geosci. Model Dev.* **14**, 125–149 (2021).

45. Vervoort, P., Kirtland Turner, S., Rochholz, F. & Ridgwell, A. Earth System Model Analysis of How Astronomical Forcing Is Imprinted Onto the Marine Geological Record: The Role of the Inorganic (Carbonate) Carbon Cycle and Feedbacks. *Paleoceanogr. Paleoclimatology* **36**, (2021).

46. Krause, A. J. *et al.* Stepwise oxygenation of the Paleozoic atmosphere. *Nat. Commun.* **9**, (2018).

47. Gough, D. O. Solar interior structure and luminosity variations. *Sol. Phys.* **74**, 21–34 (1981).

48. Reinhard, C. T. *et al.* Evolution of the global phosphorus cycle. *Nature* **541**, 386–389 (2017).

49. Wang, R. *et al.* The coupling of Phanerozoic continental weathering and marine phosphorus cycle. *Sci. Rep.* **10**, (2020).

50. Bresenham, J. E. Algorithm for computer control of a digital plotter. *IBM Syst. J.* **4**, 25–30 (2010).

51. Miller, A. I. *et al.* Phanerozoic trends in the global geographic disparity of marine biotas. *Paleobiology* **35**, 612–630 (2009).

Code Availability

The coupled paleogeographic-diversification model presented here uses input data of seafloor age distributions and paleoenvironmental conditions from the siwill22/agegrid-0.1 v1-

alpha paleogeographic model and the cGENIE Earth System Model, respectively. We provide code availability for each of these two models. The code for the paleogeographic model reconstructing seafloor age distributions from GPlates full-plate tectonic reconstructions is assigned a DOI: 10.5281/zenodo.3271360. The code for the version of the 'muffin' release of the cGENIE Earth System Model used in this study, is tagged as v0.9.20, and is assigned a DOI: 10.5281/zenodo.4618023.

The code and data for the coupled paleogeographic-diversification (INDITEK) model are available on GitHub (**https://github.com/CarmenGarciaComas/INDITEK**, last access: October 2021).The model is written in MATLAB 2013b and tested with MATLAB 2021a in a MacOS 2.3 GHz 8-Core Intel Core i9, and with MATLAB 2020b on Windows with a 2.5 GHz Intel i5-3210M and on Linux Debian with a 2.6 GHz Intel Core 9th Gen i9-9980HK processor. A manual (README.md) detailing the main code modules, basic model configuration, input data files (including those required from the paleogeographic model and the cGENIE Earth System model simulations), and how to run the model and plot the results is provided through the link above.

Acknowledgements

This work was funded by national research grants CGL2017-91489-EXP (INDITEK project) and CTM2017-87227-P (SPEAD project) from the Spanish government. A.P. acknowledges funding from the European Union's Horizon research and innovation programme under the Marie Sklodowska-Curie grant agreement No. 838373. A.R. acknowledges NSF grant EAR-2121165, as well as support from the Heising-Simons Foundation. P.C., C.G-C. and G.L. acknowledge support for the publication fee by the CSIC Open Access Publication Support Initiative through its Unit of Information Resources for Research (URICI).

Author contributions

P.C. and C.G-C. proposed the study. P.C., C.G-C. and S.M.V. developed the diversification model. A.P. and A.R. performed the cGENIE model simulations. S.W. and R.D.M. performed the plate tectonic/paleo-elevation model simulations. C.G-C. performed the coupling of the diversification model to the plate tectonic/paleo-elevation model. C.G-C. and G.L-G. developed the method to estimate global diversity from regional diversity. P.C., C.G-C., A.P., S.W., M.J.B., G.L-G., R.D.M., A.R. and S.M.V. contributed to data analysis and discussion of results. P.C., C.G-C., A.P., S.W. wrote the manuscript with inputs from all authors.

Competing interests

The authors declare no competing interests.

Supplementary Information is available for this paper.

Correspondence and requests for materials should be addressed to P.C. (pedrocermeno@icm.csic.es) and/or C.G-C. (cgcomas@icm.csic.es)

Reprints and permissions information is available at www.nature.com/reprints.

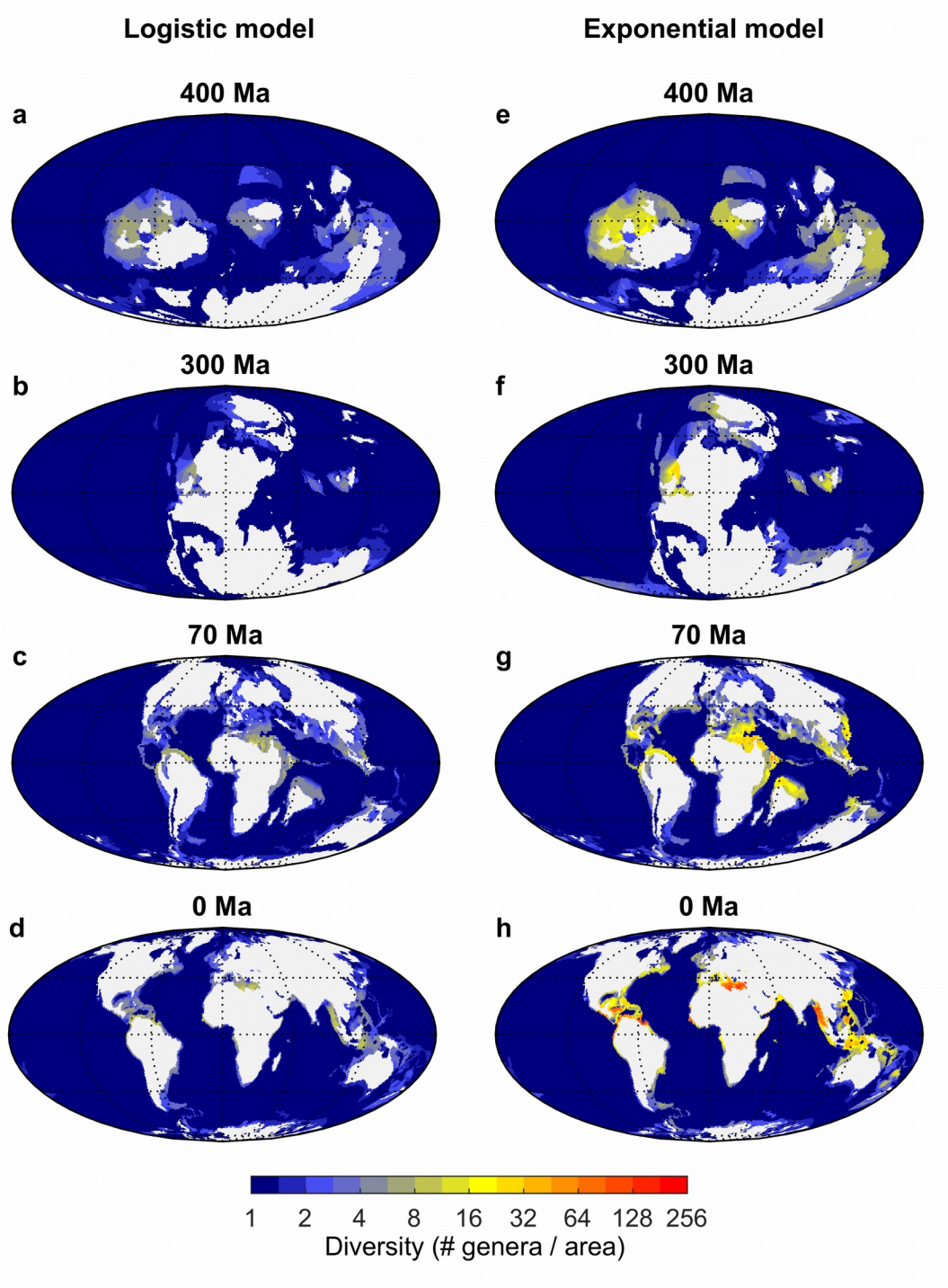

FIGURE 1: Re-diversifying the Phanerozoic oceans.

a-h, Global spatial distributions of marine benthic animal diversity (# genera / area) during the Early Devonian (Emsian, 400 Ma), Late Carboniferous (Pennsylvanian, 300 Ma), Late Cretaceous (Maastrichtian, 70 Ma) and present generated by the logistic model (**a-d**) and the exponential model (**e-h**), after imposing the pattern of mass extinctions (i.e. percentage of diversity loss and starting time and duration of mass extinctions) extracted from the fossil

diversity curve of Sepkoski[23]. This model run uses the following parameters: Q_{10} = 1.75, K_{food} = 0.5 molC $m^{-2}y^{-1}$, net diversification rate limits (ρ_{min} - ρ_{max}) = 0.001-0.035 Myr^{-1} (per capita), and a global range of carrying capacities (K_{min} and K_{max}) of 4 and 16 genera per unit area, respectively (***Supplementary Table 1***). This range of carrying capacity values is arbitrarily selected to emphasize the differences between the logistic model and the exponential model. The same plots but after imposing the mass extinction patterns extracted from the fossil diversity curves of Alroy[24] and Zaffos et al[25] are shown in ***Extended Data Figures 1*** **and** ***2***, respectively. See also ***Supplementary Videos 1-2*** (***password****: video2021*) for the full Phanerozoic sequences.

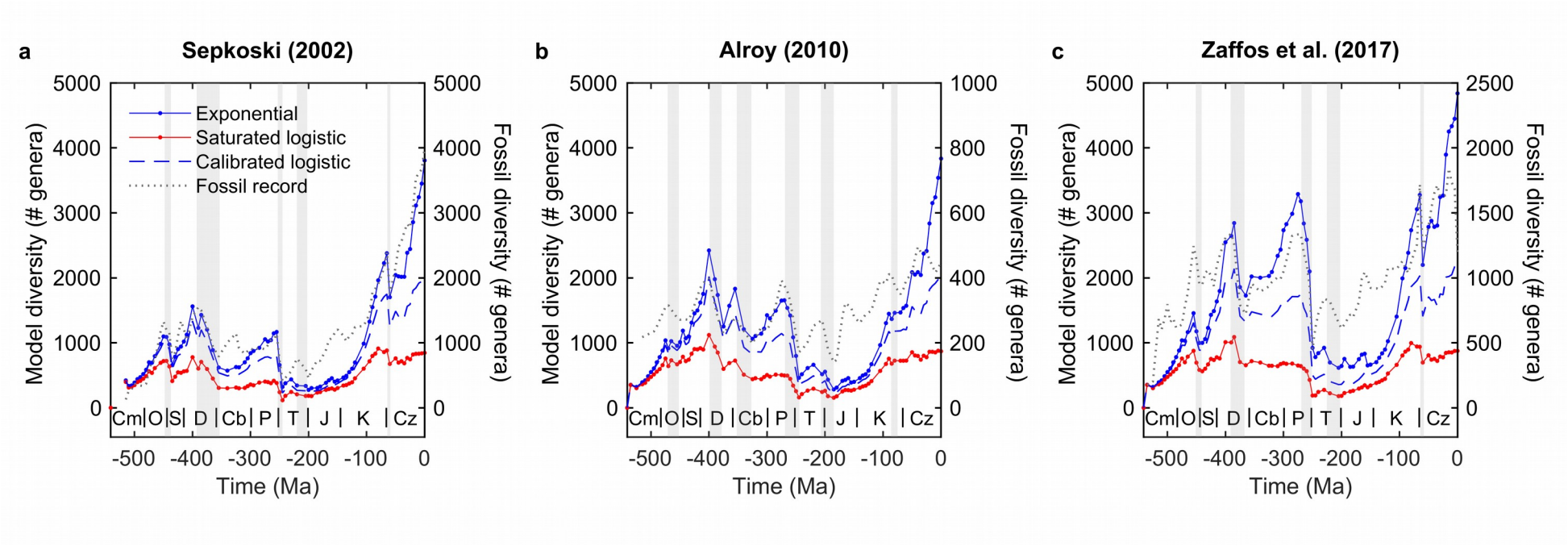

770 **FIGURE 2: Global diversity dynamics across the Phanerozoic**.

771 **a-c**, Global diversity dynamics reconstructed from the logistic model (red), the exponential model (blue) and the 'calibrated' logistic model (blue
772 dashed line, see Figure 3 for calibration) after imposing the pattern of mass extinctions (i.e. percentage of diversity loss and starting time and duration
773 of mass extinctions) of Sepkoski[23] (**a**), Alroy[24](**b**), and Zaffos et al.[25] (**c**). In each panel, the corresponding fossil diversity curve is superimposed (grey).
774 Cm, Cambrian; O, Ordovician; S, Silurian; D, Devonian; Cb, Carboniferous; P, Permain; T, Triassic; J, Jurassic; K, Cretaceous; Cz, Cenozoic.
775 Shaded areas represent mass extinction events.

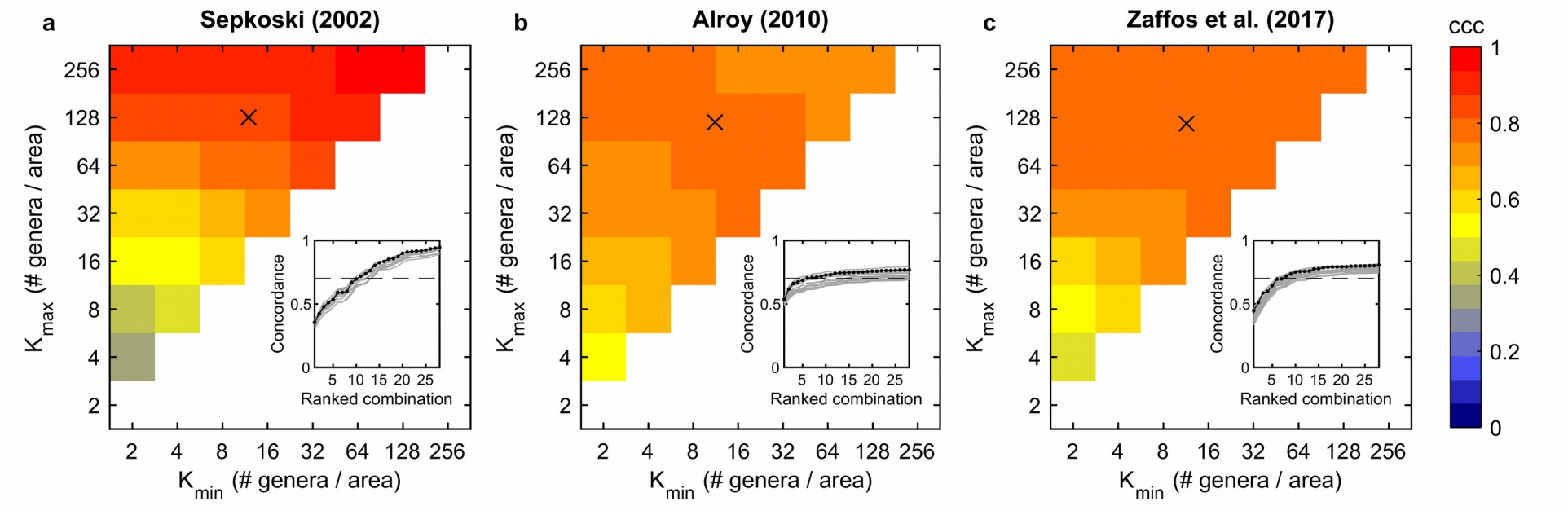

FIGURE 3: Calibrating the logistic model's carrying capacities.

a-c, Lin's concordance correlation coefficients (CCC) for the relationship between the global diversities resulting from the model and the fossil diversity estimates of Sepkoski[25] (**a**), Alroy[24] (**b**), and Zaffos et al[25] (**c**) using different combinations of K_{min} and K_{max} values in the model. See ***Extended Data Figs. 5, 6 and 7*** for details on these relationships. The inset in each panel shows the CCCs in ascending order for the different combinations of K_{min} and K_{max}. The black curve in the insets is for the simulation run using the selected parameters (***Supplementary Table 1***). The grey curves are for each of the first fifteen combinations of parameters listed in ***Extended Data Table 1***. The dashed line denotes the CCC value of 0.7 and the cross in each panel is the average of all K_{min} and K_{max} combinations giving a CCC greater than 0.7.

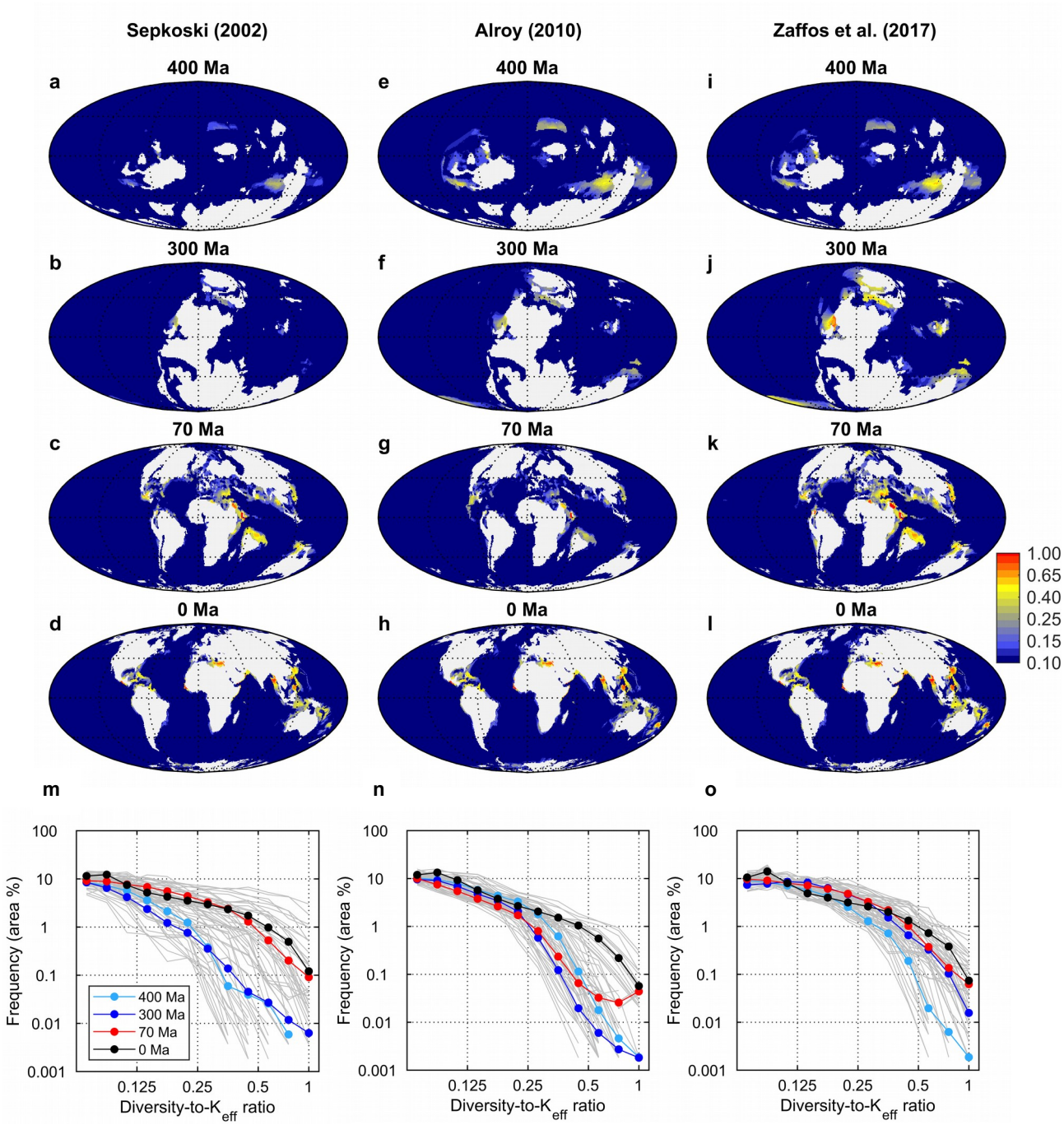

FIGURE 4: The pervasiveness of ecological unsaturation.

a-l, Spatial distribution maps of the diversity-to-carrying capacity (K_{eff}) ratio (colorbar) in deep sea habitats and flooded continental regions of the Early Devonian (Emsian, 400 Ma), Late Carboniferous (Pennsylvanian, 300 Ma), Late Cretaceous (Maastrichtian, 70 Ma) and present using the 'calibrated' logistic model after imposing the mass extinction patterns of Sepkoski[23] (**a-d**), Alroy[24] (**e-h**), and Zaffos et al[25] (**i-l**). See ***Supplementary Video 4*** (***password**: video2021*) for the full Phanerozoic sequences. **m-o**, Frequency distributions (%

area) of the diversity-to-K_{eff} ratio for the flooded continental regions. The grey lines are frequency distributions generated from simulations using the different parameter settings listed in ***Extended Data Table 1***. The colour dots are average values for different Phanerozoic times. Only the values of diversity-to-K_{eff} ratio > 0.05 are shown. For the full range of values see ***Extended Data Fig. 8***.

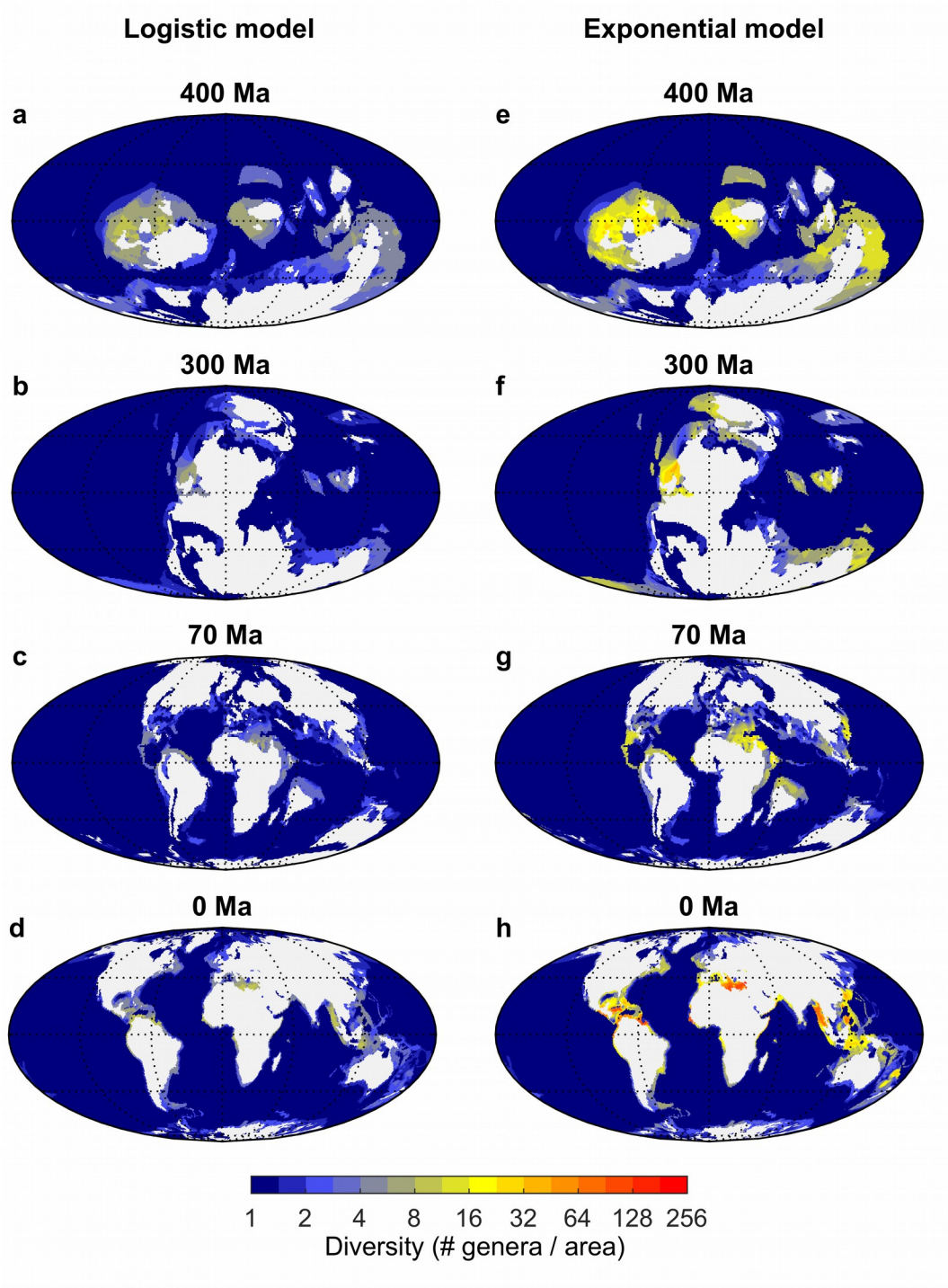

EXTENDED DATA FIGURE 1: Re-diversifying the Phanerozoic oceans. a-h, Global spatial distributions of marine benthic animal diversity during the Early Devonian (Emsian, 400 Ma), Late Carboniferous (Pennsylvanian, 300 Ma), Late Cretaceous (Maastrichtian, 70 Ma) and present generated by the logistic model (**a-d**) and the exponential model (**e-h**), after imposing the pattern of mass extinctions (i.e. percentage of diversity loss and starting time and duration of mass extinctions) extracted from the fossil diversity curve of Alroy[24]. This

model run uses the following parameter values: Q_{10} = 1.75, K_{food} = 0.5 molC $m^{-2}y^{-1}$, diversification rate limits (ρ_{min}, ρ_{max}) = 0.001, 0.035 per capita, and carrying capacities (K_{min} and K_{max}) in the range 4 to 16 genera per unit area, respectively (***Supplementary Table 1***). These K_{min} and K_{max} values are arbitrarily selected to emphasize the differences between the saturated logistic model and the exponential model. See ***Supplementary Videos 1-2*** (***password****: video2021*) for the complete Phanerozoic sequences.

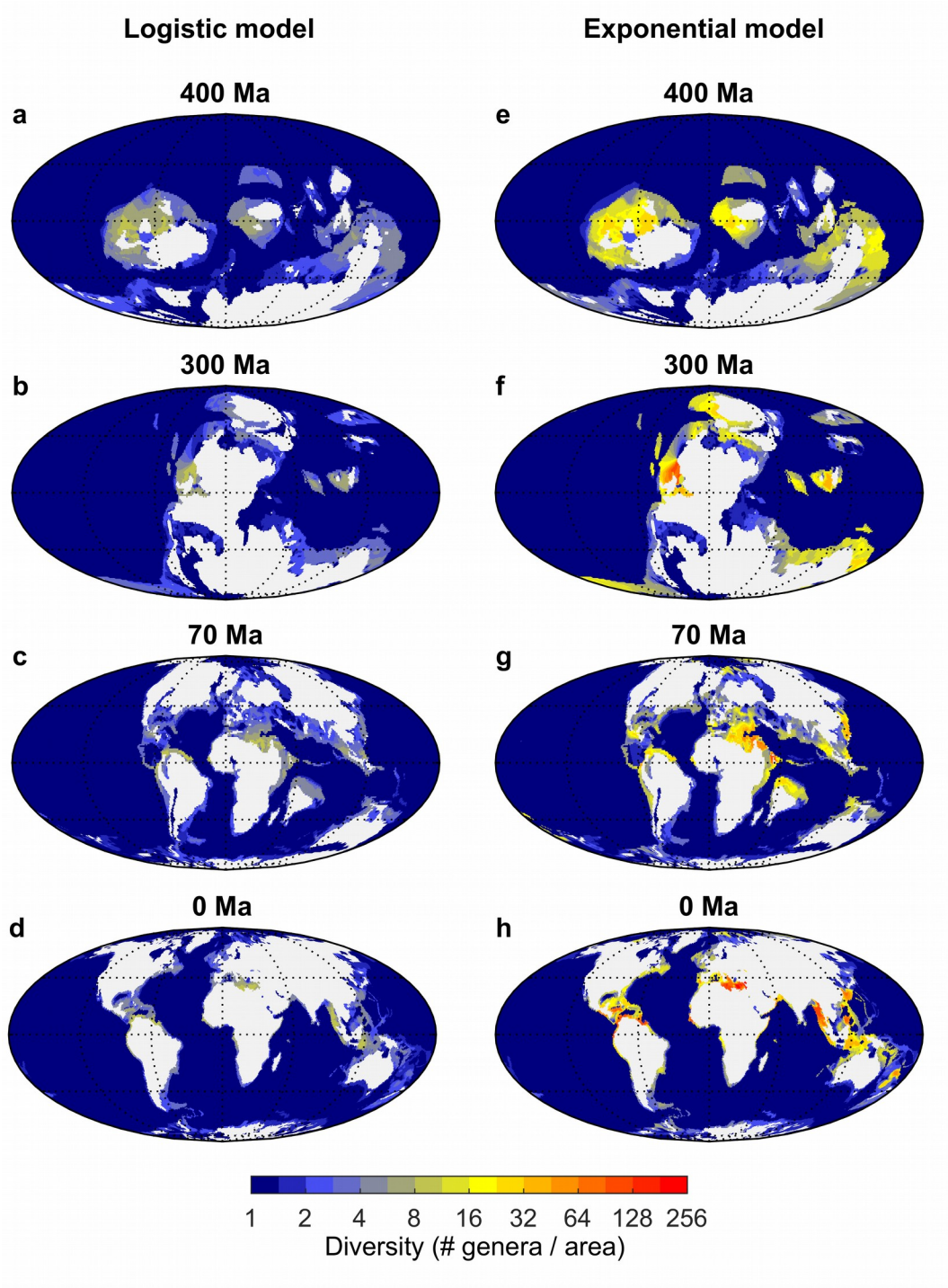

EXTENDED DATA FIGURE 2: Re-diversifying the Phanerozoic oceans. a-h, As Extended Data Figure 1 but for the pattern of mass extinctions (i.e., percentage of diversity loss, starting time and duration of mass extinction events) extracted from the global diversity curve of Zaffos et al[25]. See ***Supplementary Videos 1-2*** (***password****: video2021*) for the complete Phanerozoic sequences.

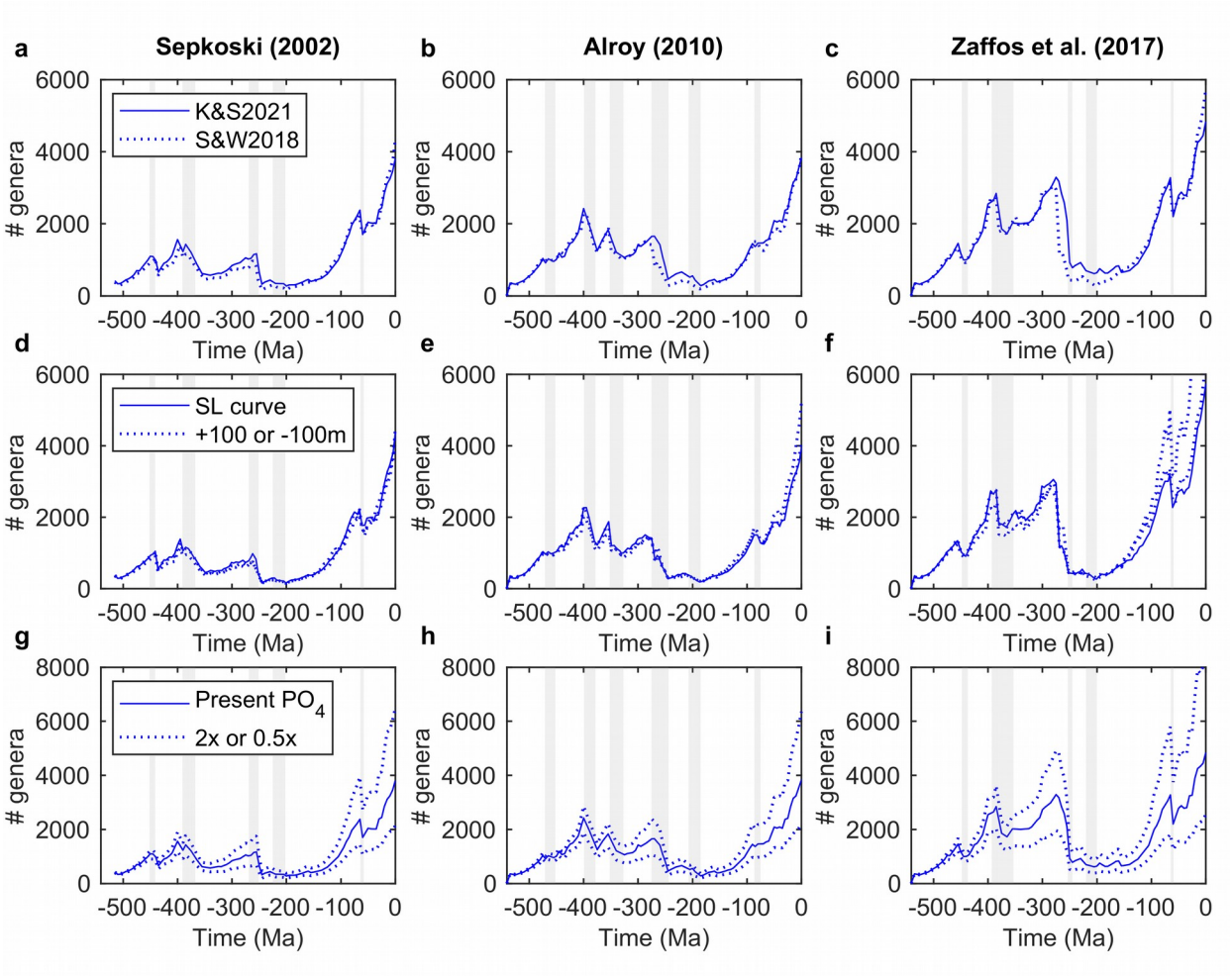

EXTENDED DATA FIGURE 3: Testing the effect of different model configurations and parameter values (sensitivity analyses). a-c, Global diversity dynamics (# genera) reconstructed using the exponential model for two alternative paleogeographic reconstructions, Koksis and Scotese[32] (KS2020) and Scotese and Wright[37] (SW2018). **d-f**, Effect of changing the sea level (+/- 100 m with respect to the paleoshoreline reported in Kocsis and Scotese[32]) on Phanerozoic dynamics of diversity. **g-i**, Effect of changing the ocean phosphate concentration (x2 and x0.5 with respect to present day concentrations, i.e., default scenario) on global diversity dynamics. Shaded areas indicate mass extinctions.

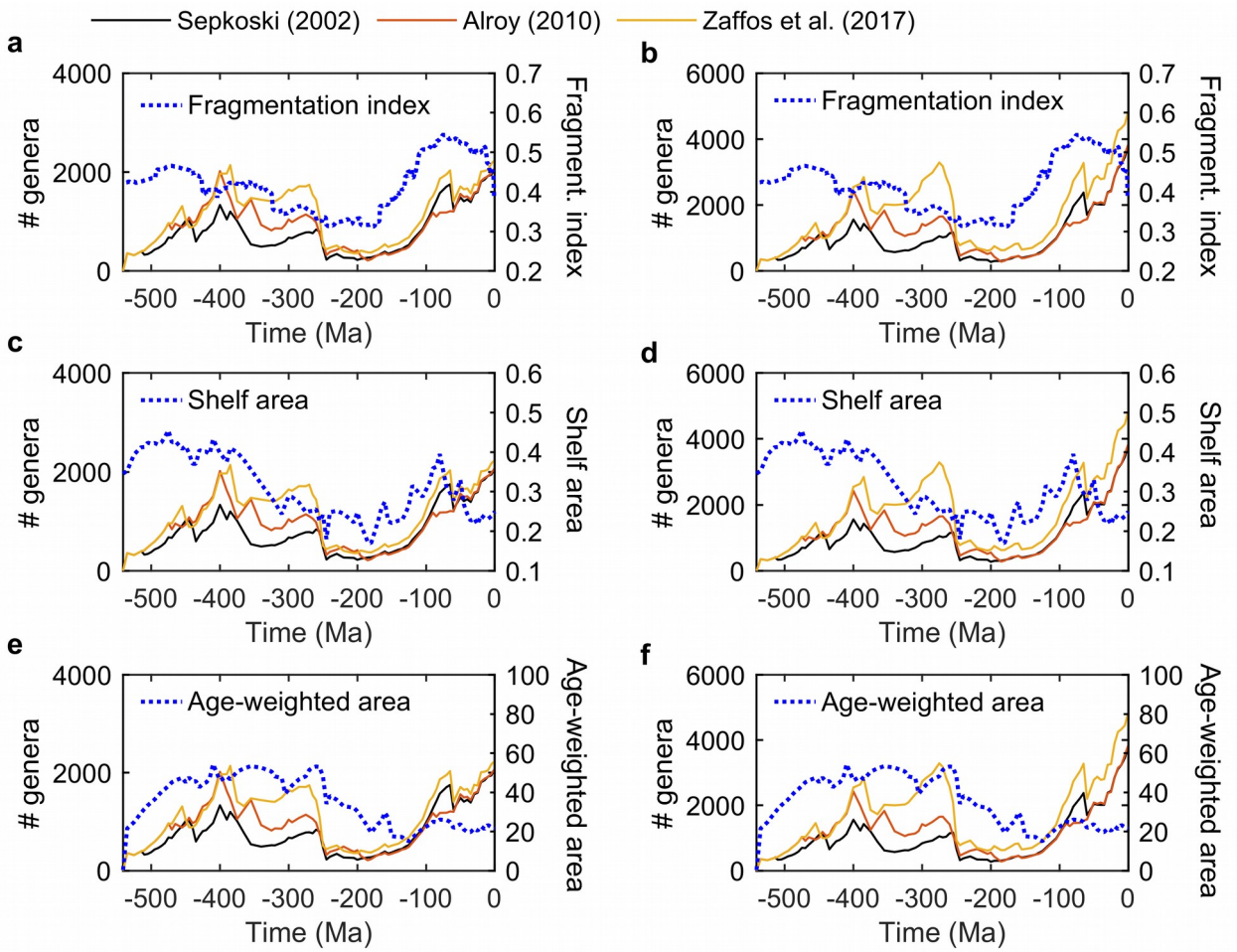

EXTENDED DATA FIGURE 4: Continental configuration and global diversity dynamics. a-f, Global diversity dynamics (# genera) reconstructed from the 'calibrated' logistic model (**a, c, e**) and the exponential model (**b, d, f**) overimposed on the temporal variability of the fragmentation index (**a, b**), global mean shelf area (**c, d**) and mean age-weighted area (**e, f**).

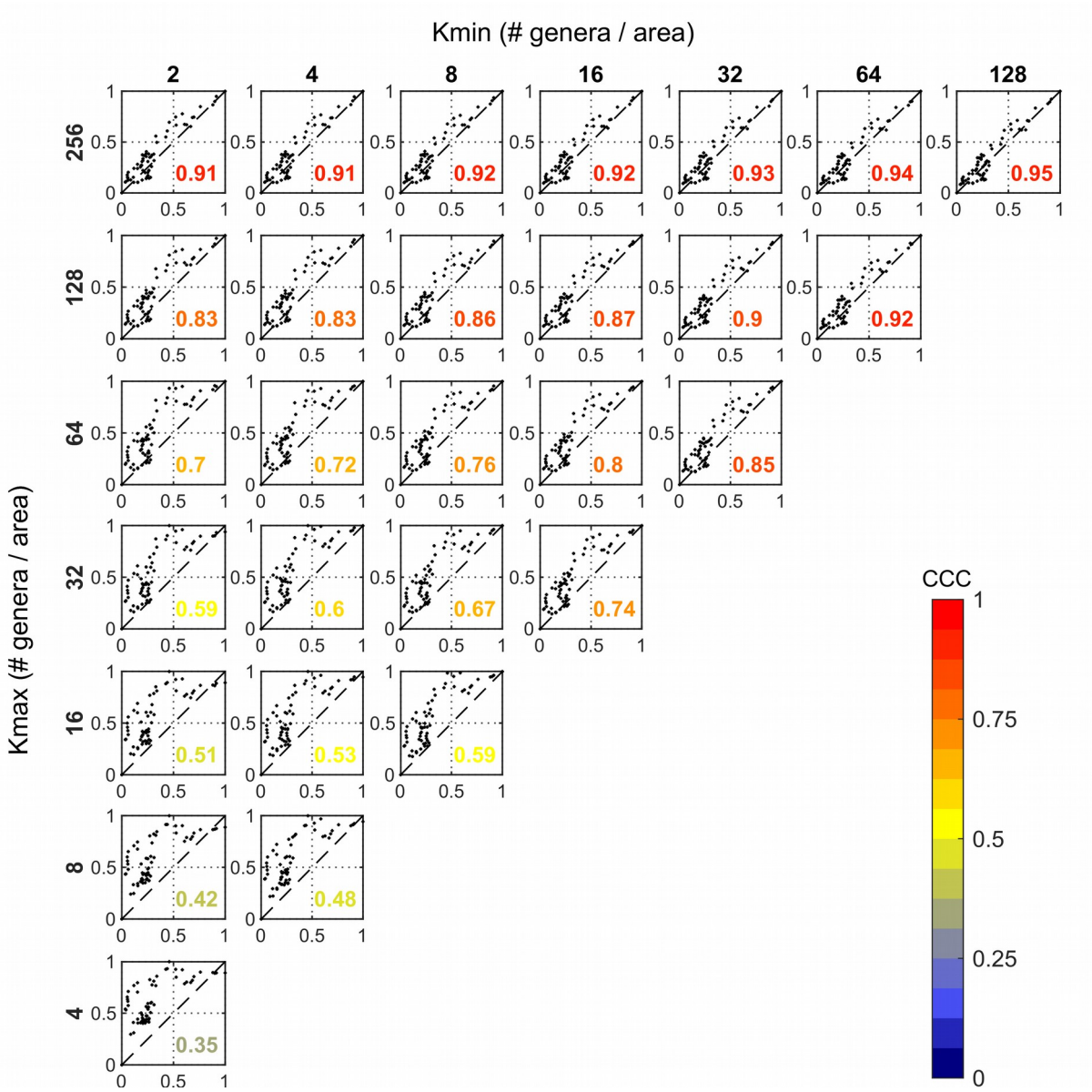

EXTENDED DATA FIGURE 5: Calibrating the K_{min} and K_{max} values of the logistic model. Normalized model diversity (0-1) versus normalized fossil diversity (0-1) for different combinations of the K_{min} and K_{max} values of the model. These simulations use the pattern of mass extinctions extracted from the fossil diversity curve of Sepkoski[23]. The Concordance Correlation coefficient (CCC), which quantifies the alignment of the model estimates to the 1:1 line, is shown in each panel with color code.

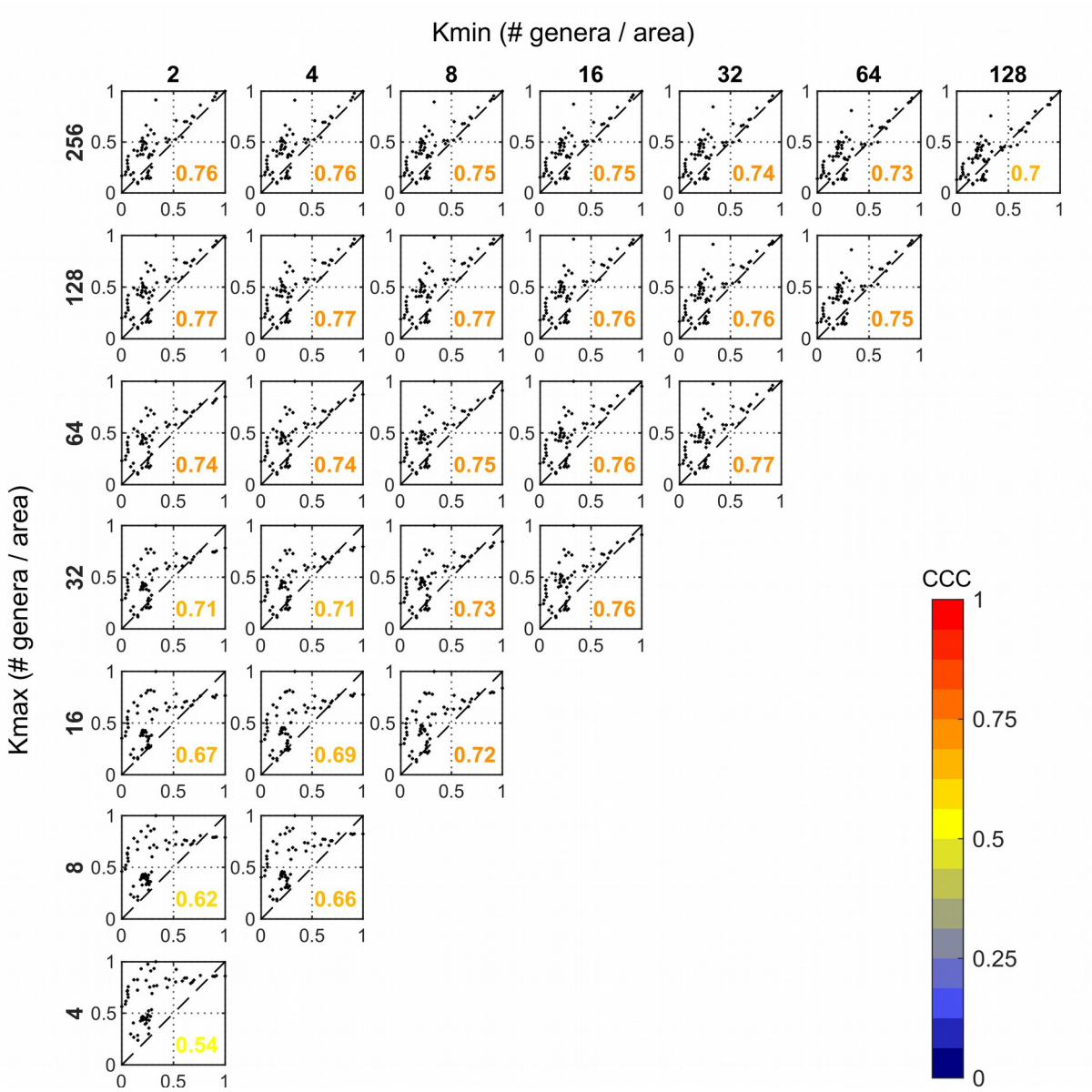

EXTENDED DATA FIGURE 6: Calibrating the K_{min} and K_{max} values of the logistic model. As Extended Data Figure 5 but for the pattern of mass extinctions extracted from the fossil diversity curve of Alroy[24], and the fossil diversity estimates reported in Alroy.

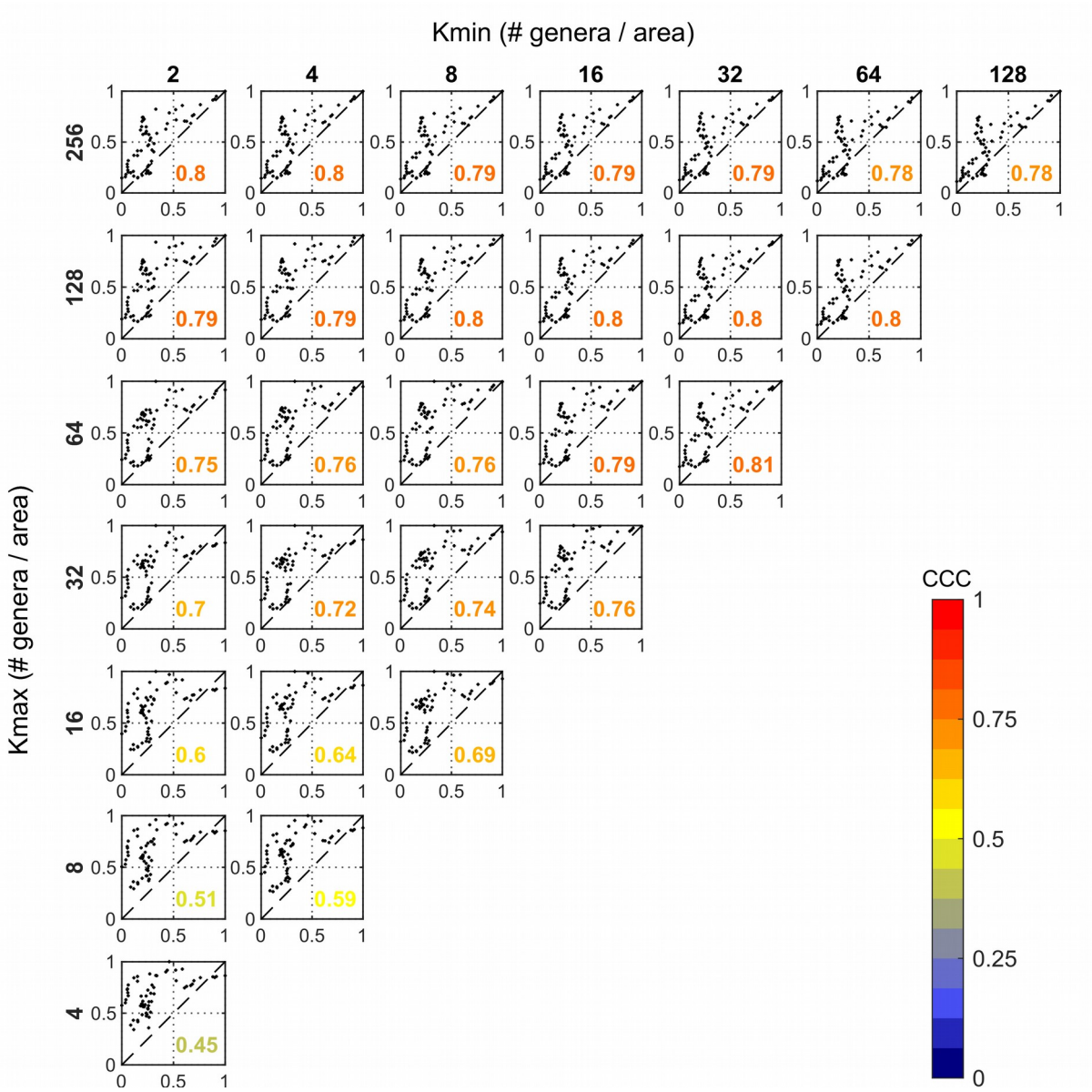

EXTENDED DATA FIGURE 7: Calibrating the K_{min} and K_{max} values of the logistic model. As Extended Data Figure 5 but for the pattern of mass extinctions extracted from the fossil diversity curve of Zaffos et al[25] and the fossil diversity estimates reported in Zaffos et al[25].

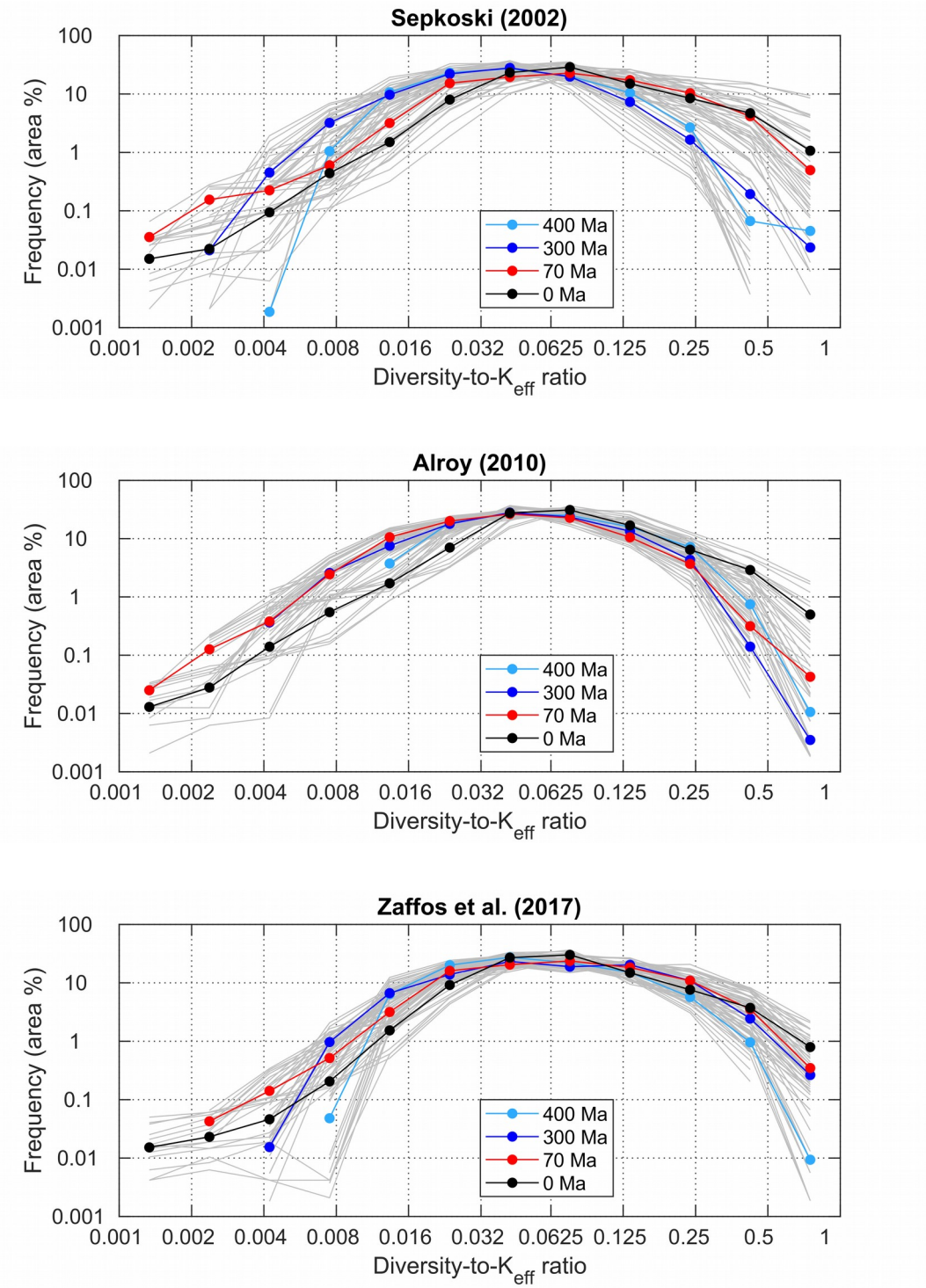

EXTENDED DATA FIGURE 8: Full range of the diversity-to-K_{eff} frequency distribution pattern. Data lower than 0.0625 are shown here but excluded from main Fig. 4. This is to expand the details of the range of values approaching saturation levels in the main body of this article.

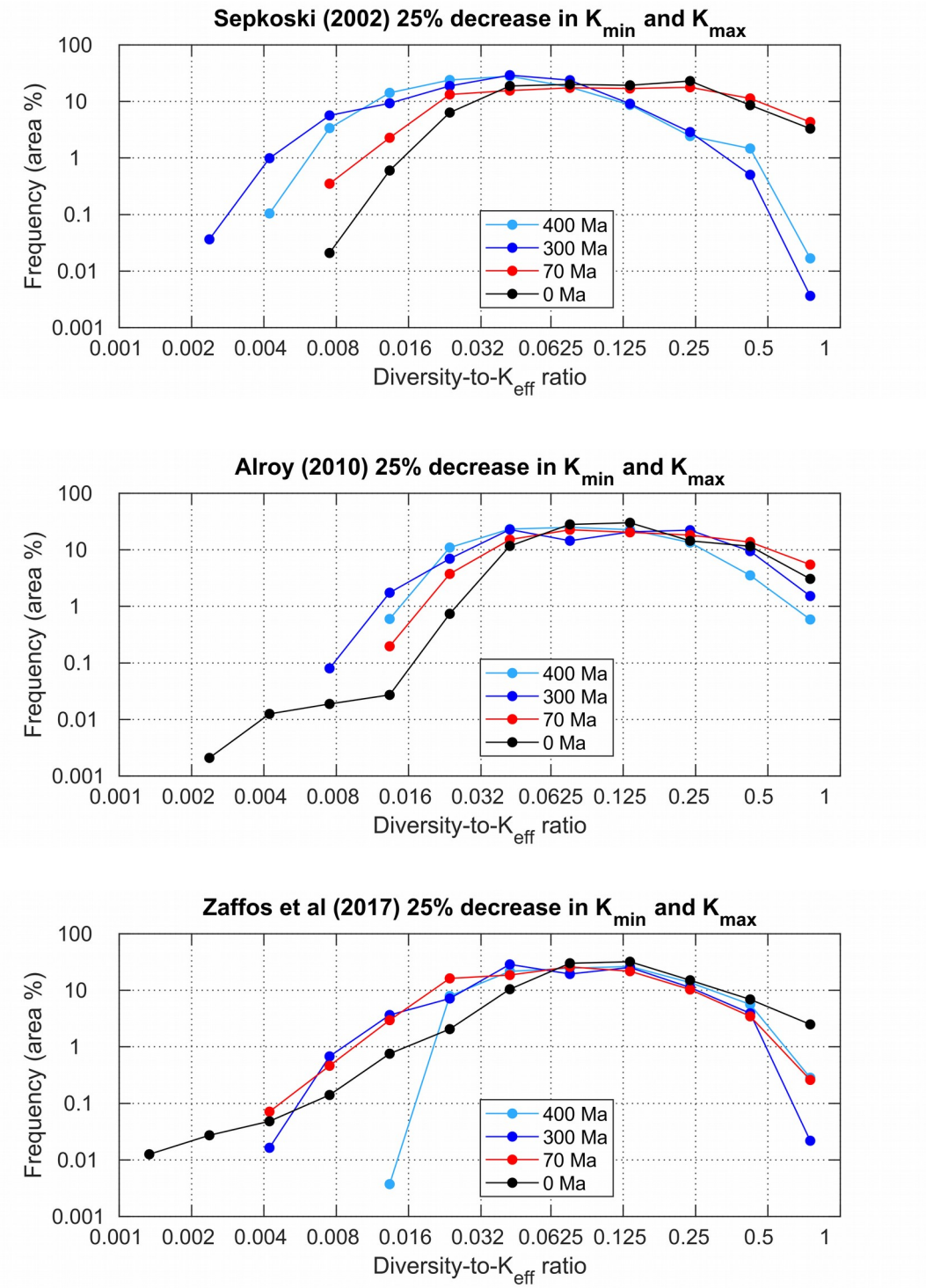

EXTENDED DATA FIGURE 9: Robustness of the diversity-to-K_{eff} frequency distribution pattern. Frequency distributions (% area) of the diversity-to-K_{eff} ratio for the flooded continental regions after decreasing the values of K_{min} and K_{max} in the model by 25% with respect to the calibrated values [i.e., crosses in ***Fig. 3***; K_{min}-K_{max}: 12-128 (for Sepkoski), 11-118 (for Alroy), 11-117 (for Zaffos et al.)].

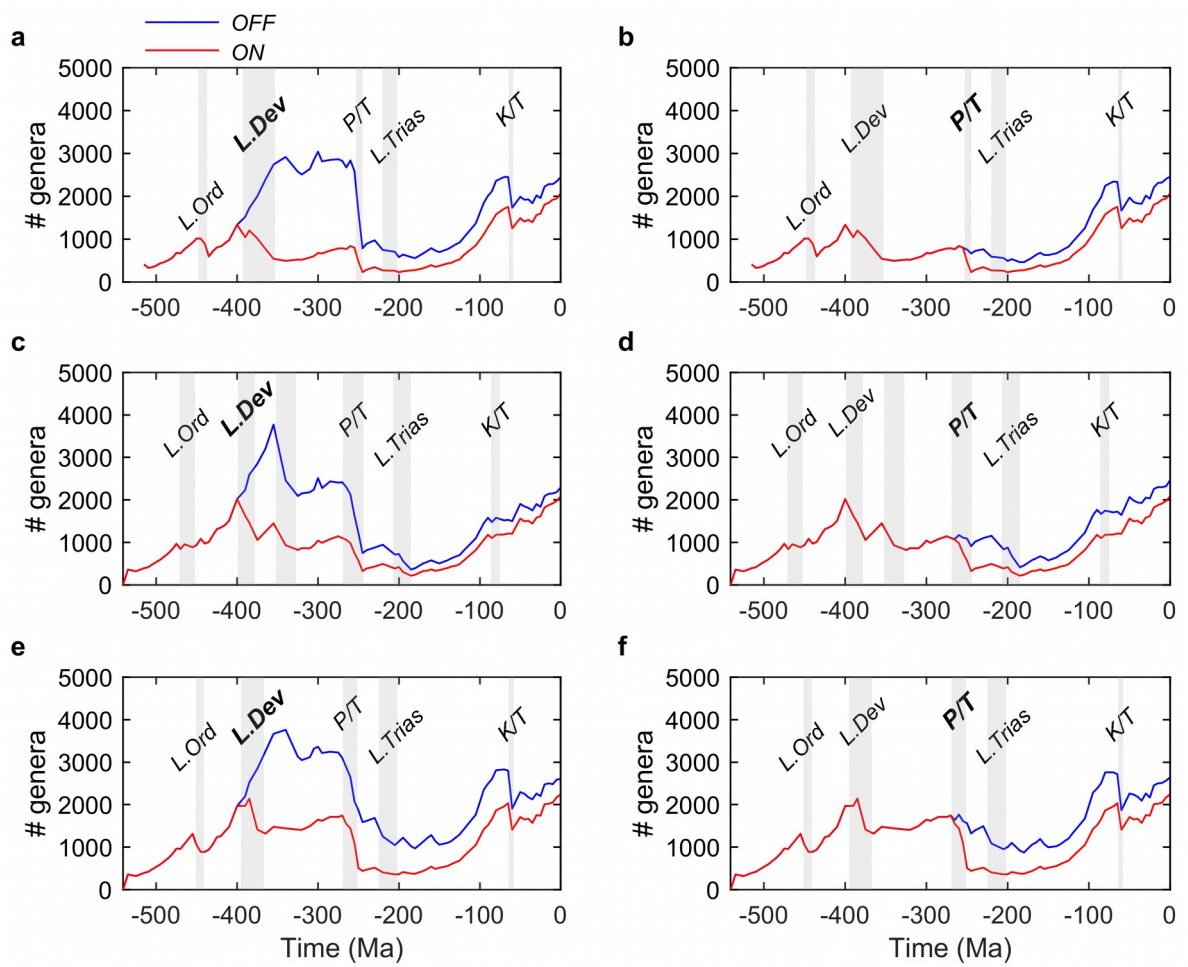

EXTENDED DATA FIGURE 10: Testing the effect of enabling/disabling mass extinctions. a-f, Global diversity (# genera) trajectories reconstructed from the 'calibrated' logistic model after disabling (blue) and enabling (red) the Late Devonian and Permo-Triassic mass extinctions from the mass extinction pattern of Sepkoski[23] (**a, b**), Alroy[24] (**c, d**) and Zaffos et al[25] (**e, f**), respectively. The mass extinctions marked in bold represent those disabled/enabled in each panel.

EXTENDED DATA TABLE 1. Lin's Concordance Correlation Coefficient (CCC) using different parameter settings in the model.

SEPKOSKI 2002					ALROY 2010					ZAFFOS et al 2017				
Model parameters			Lin's CCC*		Model parameters			Lin's CCC*		Model parameters			Lin's CCC*	
Q10	*kfood*	*ρmax*	Exp	Log	*Q10*	*kfood*	*ρmax*	Exp	Log	*Q10*	*kfood*	*ρmax*	Exp	Log
2	0.25	0.035	0.96	0.46	1.5	1	0.035	0.73	0.64	1.5	1	0.035	0.78	0.64
1.75	0.25	0.035	0.96	0.48	1.5	0.75	0.035	0.71	0.66	1.75	1	0.035	0.77	0.60
1.5	0.5	0.035	0.96	0.48	1.75	1	0.035	0.70	0.60	1.75	0.75	0.035	0.76	0.63
2.25	0.25	0.035	0.96	0.45	1.75	0.75	0.035	0.70	0.62	2	1	0.035	0.75	0.57
1.5	0.25	0.035	0.96	0.50	2	0.75	0.035	0.70	0.60	2	0.75	0.035	0.75	0.59
1.5	0.75	0.04	0.96	0.47	1.5	1	0.04	0.68	0.64	1.5	0.75	0.035	0.75	0.66
1.75	0.5	0.04	0.96	0.46	2	1	0.035	0.68	0.58	2.25	1	0.035	0.74	0.55
1.5	0.5	0.04	0.96	0.48	1.5	0.5	0.035	0.68	0.69	2.25	0.75	0.035	0.74	0.57
2	0.5	0.04	0.95	0.44	1.75	0.5	0.035	0.68	0.65	2.5	1	0.035	0.74	0.53
2.25	0.5	0.04	0.95	0.43	2	0.5	0.035	0.67	0.62	2.5	0.75	0.035	0.73	0.56
2.5	0.25	0.035	0.95	0.48	2.25	0.75	0.035	0.68	0.60	1.75	0.5	0.035	0.72	0.63
1.75	0.75	0.04	0.95	0.44	2.5	0.75	0.035	0.68	0.59	2.5	0.5	0.035	0.72	0.58
1.75	0.5	0.035	0.95	0.45	2.5	1	0.035	0.68	0.56	2.25	0.5	0.035	0.72	0.59
1.5	1	0.04	0.95	0.46	2	1	0.04	0.67	0.58	1.75	1	0.04	0.72	0.61
2	0.75	0.04	0.95	0.42	2.25	1	0.035	0.66	0.57	1.5	1	0.04	0.72	0.65
2.25	0.75	0.04	0.94	0.40	2.5	1	0.04	0.66	0.56	2	0.5	0.035	0.71	0.61
2.5	0.75	0.04	0.94	0.41	1.75	1	0.04	0.66	0.60	2	1	0.04	0.71	0.58
2.5	0.5	0.04	0.94	0.46	2.5	0.5	0.035	0.65	0.62	2.25	1	0.04	0.70	0.56
2	0.5	0.035	0.94	0.43	2.25	1	0.04	0.65	0.57	2.5	1	0.04	0.70	0.55
2.5	0.5	0.035	0.94	0.46	2.25	0.5	0.035	0.65	0.61	1.5	0.5	0.035	0.69	0.67
2.25	0.5	0.035	0.94	0.42	1.5	0.75	0.04	0.64	0.66	1.75	0.75	0.04	0.68	0.62
1.5	0.75	0.035	0.93	0.47	1.75	0.75	0.04	0.64	0.62	2.5	0.75	0.04	0.67	0.56
1.75	1	0.04	0.93	0.43	2	0.75	0.04	0.63	0.59	2	0.75	0.04	0.67	0.59
2.25	0.25	0.04	0.93	0.44	2	0.25	0.035	0.62	0.65	2.25	0.75	0.04	0.67	0.57
2	0.25	0.04	0.93	0.45	1.75	0.25	0.035	0.62	0.67	2.5	0.25	0.035	0.66	0.60
1.75	0.25	0.04	0.92	0.46	2.5	0.25	0.035	0.62	0.63	1.5	0.75	0.04	0.65	0.67
2.5	1	0.04	0.92	0.42	2.25	0.75	0.04	0.61	0.57	2.25	0.25	0.035	0.65	0.62
2	1	0.04	0.92	0.41	2.5	0.75	0.04	0.60	0.58	2	0.25	0.035	0.64	0.63
2.5	0.25	0.04	0.92	0.47	2.25	0.25	0.035	0.60	0.65	2.5	0.5	0.04	0.63	0.57
1.5	0.25	0.04	0.92	0.48	1.5	0.25	0.035	0.60	0.69	2.25	0.5	0.04	0.62	0.59
1.75	0.75	0.035	0.91	0.43	1.75	0.5	0.04	0.59	0.65	1.75	0.25	0.035	0.62	0.65
2.25	1	0.04	0.91	0.40	2	0.5	0.04	0.59	0.62	2	0.5	0.04	0.62	0.60
2	0.75	0.035	0.89	0.41	1.5	0.5	0.04	0.58	0.68	1.75	0.5	0.04	0.61	0.63
2.5	0.75	0.035	0.89	0.42	2.5	0.5	0.04	0.57	0.60	1.5	0.25	0.035	0.58	0.68
1.5	1	0.035	0.89	0.45	2.25	0.5	0.04	0.56	0.60	1.5	0.5	0.04	0.57	0.67
2.25	0.75	0.035	0.88	0.39	2	0.25	0.04	0.52	0.64	2.5	0.25	0.04	0.54	0.59
1.75	1	0.035	0.85	0.41	1.5	0.25	0.04	0.51	0.69	2.25	0.25	0.04	0.53	0.60
2	1	0.035	0.83	0.40	1.75	0.25	0.04	0.51	0.66	2	0.25	0.04	0.51	0.62
2.5	1	0.035	0.83	0.41	2.5	0.25	0.04	0.51	0.62	1.75	0.25	0.04	0.51	0.64
2.25	1	0.035	0.81	0.39	2.25	0.25	0.04	0.50	0.63	1.5	0.25	0.04	0.47	0.68

*The CCCs are for the relationship between the normalized diversities estimated from the fossil record and those generated by the exponential (Exp) and the logistic (Log) models. The fifteen combinations of model parameters that gave the highest CCC for each mass extinction pattern were selected. Of these, the combination that gave the highest CCC for the relationship between the fossil diversities and the diversities generated by the calibrated logistic (Cal. Log) model was selected as the best (Extended Data Table 1 continued).

859 **EXTENDED DATA TABLE 1.** (Continued).

SEPKOSKI 2002				ALROY 2010				ZAFFOS et al 2017			
Model parameters			Lin's CCC	Model parameters			Lin's CCC	Model parameters			Lin's CCC
Q10	*kfood*	*ρmax*	Cal. Log	*Q10*	*kfood*	*ρmax*	Cal. Log	*Q10*	*kfood*	*ρmax*	Cal. Log
1.5	0.25	0.035	0.95	1.5	0.5	0.035	0.80	1.5	0.75	0.035	0.82
1.5	0.5	0.035	0.95	1.5	0.75	0.035	0.77	1.5	1	0.04	0.81
1.5	0.75	0.04	0.95	**1.75**	**0.5**	**0.035**	**0.77***	**1.75**	**0.5**	**0.035**	**0.81***
2	0.5	0.04	0.94	1.5	1	0.04	0.76	1.5	1	0.035	0.80
2	0.25	0.04	0.94	1.5	1	0.035	0.75	1.75	0.75	0.035	0.79
1.75	**0.5**	**0.035**	**0.94***	1.75	0.75	0.035	0.75	2.25	0.5	0.035	0.79
1.5	0.25	0.04	0.93	2	0.75	0.035	0.73	1.75	1	0.04	0.78
1.5	0.75	0.035	0.93	2.25	0.75	0.035	0.72	1.75	1	0.035	0.78
2.25	0.75	0.04	0.93	1.75	1	0.035	0.72	2	0.75	0.035	0.78
1.75	1	0.04	0.92	2.5	0.75	0.035	0.72	2.5	0.5	0.035	0.78
1.75	0.75	0.035	0.91	2.25	1	0.04	0.71	2.25	0.75	0.035	0.77
1.5	1	0.035	0.90	2	1	0.035	0.71	2	1	0.035	0.76
2	0.75	0.035	0.89	2.5	1	0.04	0.70	2.5	0.75	0.035	0.76
2.25	0.75	0.035	0.88	2.25	1	0.035	0.69	2.25	1	0.035	0.75
2.5	0.75	0.035	0.87	2.5	1	0.035	0.69	2.5	1	0.035	0.74

860 *The bold numbers show the combination of parameters selected.

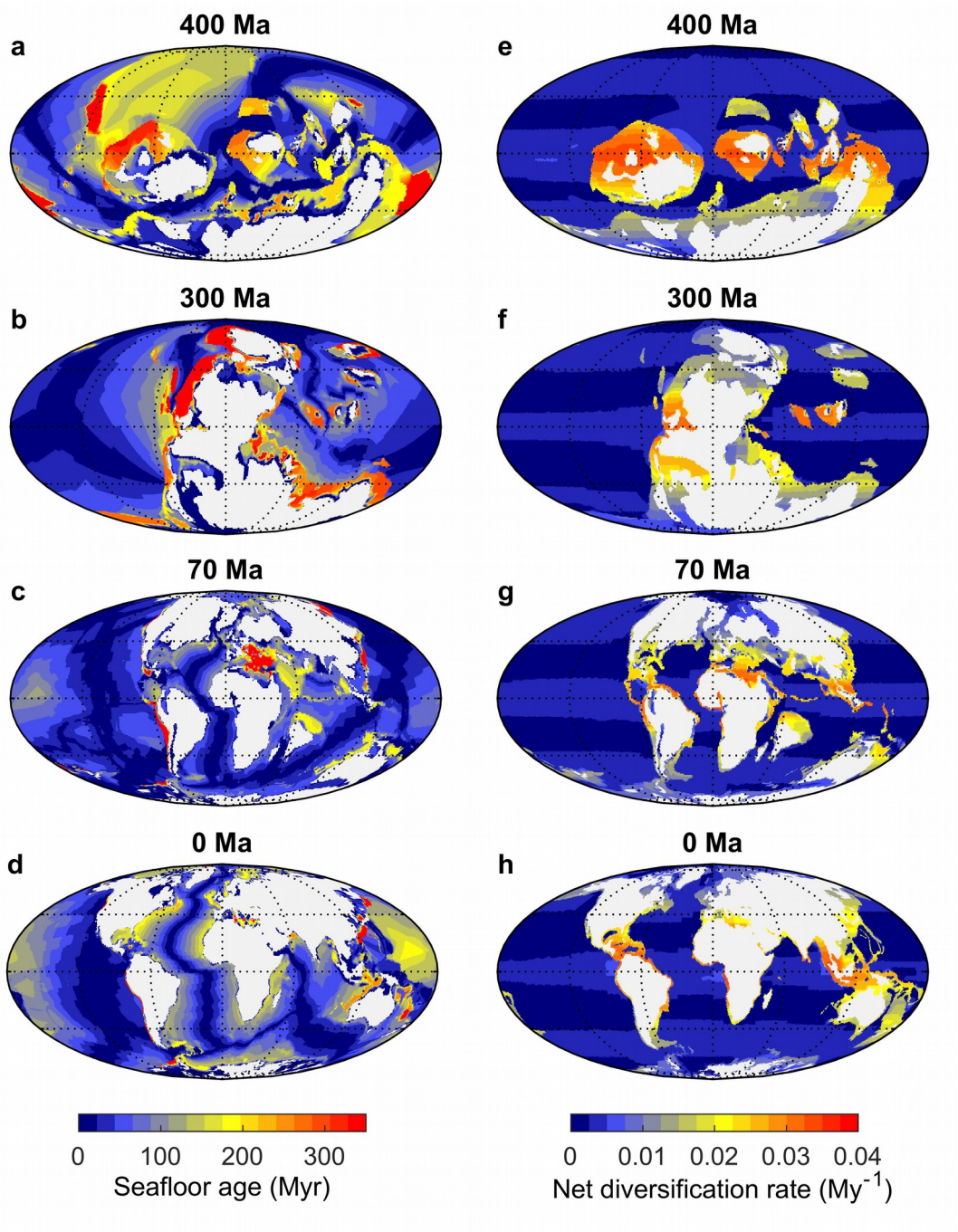

SUPPLEMENTARY FIGURE 1: Model estimates of seafloor age and net diversification rate.

a-d, Age of the seafloor in open ocean and flooded continental regions in the Early Devonian (Emsian, 400 Ma), Late Carboniferous (Pennsylvanian, 300 Ma), Late Cretaceous (Maastrichtian, 70 Ma) and present. **e-h,** Spatially-resolved net diversification rate (see Methods for details).

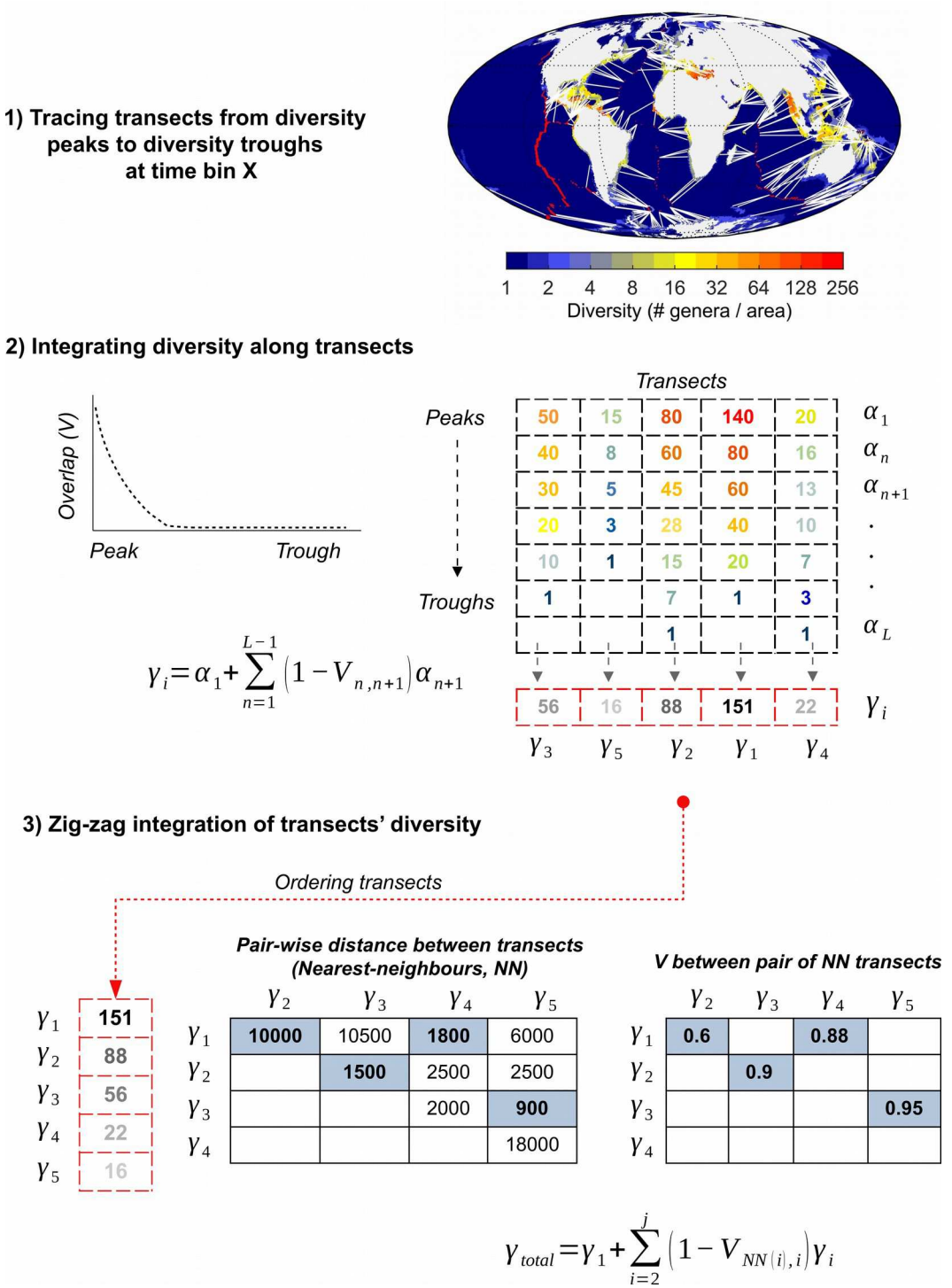

SUPPLEMENTARY FIGURE 2: Computing global diversity from diversity maps. For each time interval or regional diversity map, 1) we plot hundreds of transects (white lines) from the diversity peaks to their nearest troughs, 2) we integrate diversity along the transects (from α_n to α_L) according to the distance between pairs of grids using the overlap coefficient (V), which gives the proportion of shared genera with respect to the grid with the least

diversity, i.e., $V_{n,n+1} * min(\alpha_n; \alpha_{n+1})$ (see Annex 1), 3) we order the resulting transects' diversity (γ_i) from maximum diversity (γ_{max}) to minimum diversity (γ_{min}) and calculate the pair-wise distance between transects (their peaks), and finally 4) we integrate the diversity of transects from the greatest to lowest according to the nearest-neighbour distance of the corresponding transect to those transects already integrated (γ_{total}).

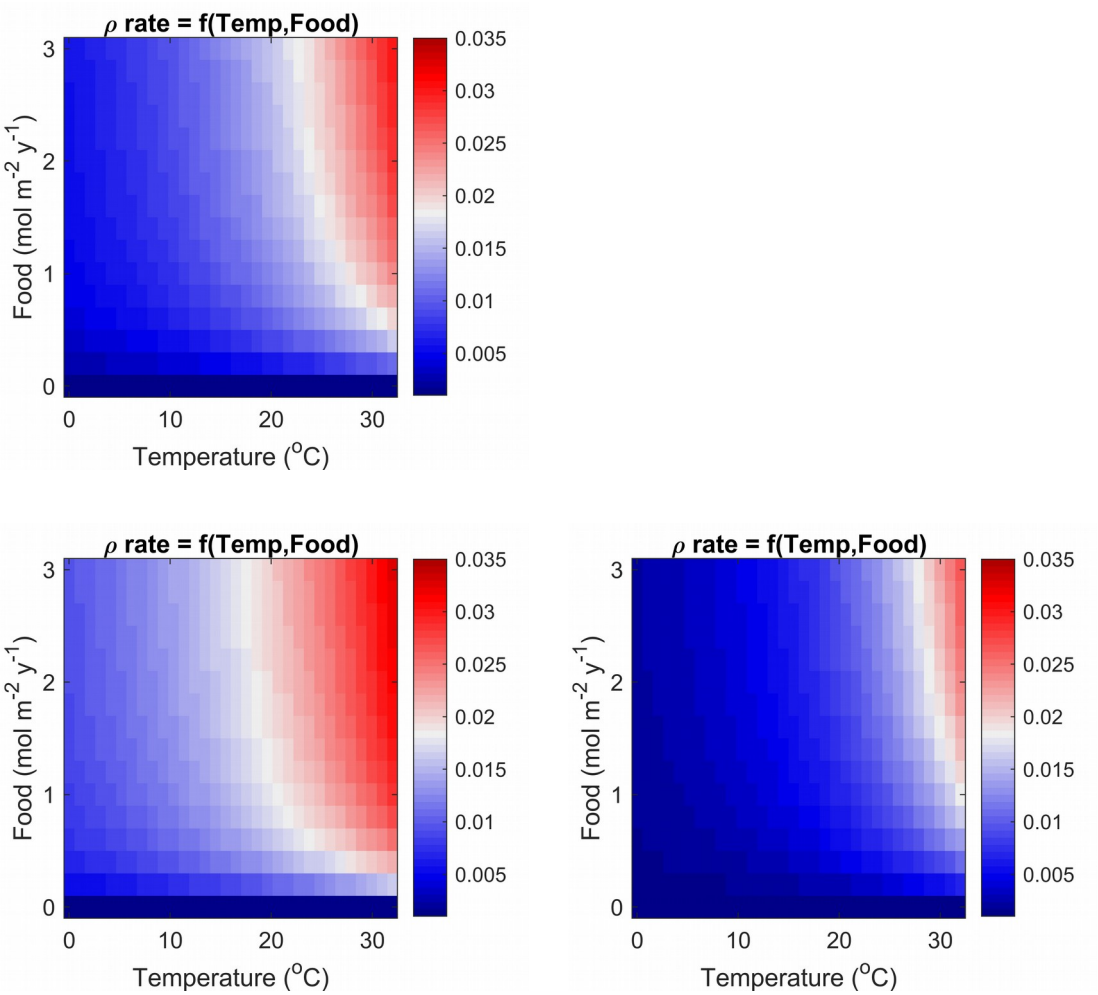

SUPPLEMENTARY FIGURE 3: Interactive effect of seawater temperature and food supply on net diversification rate.

(upper panel) Combined effect of seawater temperature and food supply on net diversification rate (ρ) for the set of parameters used to run the main simulations (i.e. Q_{10} = 1.75; K_{food} = 0.5 molC $m^{-2}y^{-1}$; ρ = 0.001 - 0.035 Myr^{-1}). (lower panels) Same as upper panel but for two extreme parameter settings (Q_{10} = 1.5; K_{food} = 0.25 molC $m^{-2}y^{-1}$; ρ = 0.001 Myr^{-1} for left the panel, and Q_{10} = 2.5; K_{food} = 1 molC $m^{-2}y^{-1}$; ρ = 0.035 Myr^{-1} for the right panel).

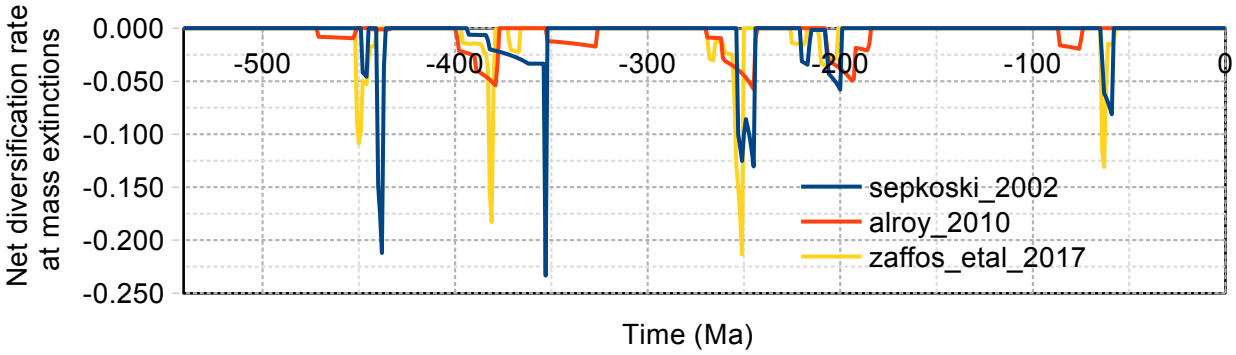

SUPPLEMENTARY FIGURE 4: Mass extinction patterns extracted from the global diversity curves of Sepkoski, Alroy and Zaffos et al. These data are provided as Source Data file 2.

SUPPLEMENTARY TABLE 1. Model parameters and range of parameter values tested.

Symbol	Description	Value	Range tested	units
ρ_{min}	Minimum net diversification rate	0.001	--	Myr^{-1}
ρ_{max}	Maximum net diversification rate	0.035	0.03 – 0.04	Myr^{-1}
Q_{10}	Thermal sensitivity	1.75	1.5 – 2.5	n.u.
K_{food}	Half-saturation constant for food	0.5	0.25 – 1	mol m^{-2} yr^{-1}
lat-lon	Radius of search for immigration	278	0 – 278	Km

SUPPLEMENTARY VIDEOS 1-4. Full Phanerozoic sequences for the spatial reconstructions of diversity based on the logistic model (1), the exponential model (2) and the 'calibrated' logistic model (3). Full Phanerozoic sequences for the spatial reconstructions of diversity-to-carrying capacity ratio (4). These videos are uploaded along with the manuscript to the journal server but can also be seen in Vimeo using the hyperlinks and password: video2021.

SOURCE DATA 1. Digitized global diversity curves from original reports.

SOURCE DATA 2. Mass extinction patterns, including the percentage of diversity loss as well as the starting time and duration of the Ordovician-Silurian (Hirnatian), Late Devonian (Frasnian-Famennian), Permian-Triassic, Late Triassic, and Cretaceous-Paleogene events, extracted from the fossil diversity curves of Sepkoski, Alroy and Zaffos et al. This data is provided as an ASCII file including four columns: 1) geological time (Ma), 2) net diversification rate (Myr^{-1}) from Sepkoski, 3) net diversification rate from Alroy, and 4) net diversification rate from Zaffos et al. See also ***Supplementary Figure 4*** for a graphical representation.

SOURCE DATA FIGURES. The source data for the figures and extended data figures presented in this article are available on GitHub (https://github.com/CarmenGarciaComas/INDITEK).

ANNEX 1. Converting Jaccard coefficient to Overlap coefficient

The Jaccard similarity index (J) is the metric most commonly used to express the similarity between two communities. Let us call the intersection of two samples $\alpha_n \cap \alpha_{n+1}$ and their union $\alpha_n \cup \alpha_{n+1}$. The cardinal (number of elements) of a set will be represented by vertical bars, i.e. $\alpha_n = |A_n|$. The Jaccard similarity (J) of α_n and α_{n+1} is then defined as the cardinal of the intersection divided by that of the union:

$$J(A_n, A_{n+1}) = \frac{|A_n \cap A_{n+1}|}{|A_n \cup A_{n+1}|} = \frac{|A_n \cap A_{n+1}|}{|A_n| + |A_{n+1}| - |A_n \cap A_{n+1}|}$$

The J index between points n and n+1 is bounded between 0 and $min(\alpha_n; \alpha_{n+1})/max(\alpha_n; \alpha_{n+1})$, where α_n; α_{n+1} are the diversities of two samples. A larger value for J ($J > 1$) would mean that there are more shared species between the two communities than there are species within the least diverse community, which is ecologically absurd. However, using a single similarity decay function can lead the computed value of J to be locally larger than $min(\alpha_n; \alpha_{n+1})/max(\alpha_n; \alpha_{n+1})$. To correct this artifact, we used the overlap coefficient (V) instead of J. The overlap coefficient is bounded between 0 and 1, whatever the ratio of diversities. Therefore, using an overlap decay function never creates artifacts.

The overlap coefficient (V), also known as the Szymkiewicz–Simpson coefficient, is defined as the cardinal of the intersection divided by that of the smallest set:

$$V(A_n, A_{n+1}) = \frac{|A_n \cap A_{n+1}|}{(min(|A_n|, |A_n + 1|))}$$

Without loss of generality, let us consider that α_{n+1} is smaller than α_n. We will call $R = \alpha_n/\alpha_{n+1}$ the ratio of the two cardinals. V can be estimated from J and vice-versa as follows:

$$V(A_n, A_{n+1}) = J(A_n, A_{n+1}) \frac{|A_n| + |A_{n+1}| - |A_n \cap A_{n+1}|}{|A_{n+1}|} = J(A_n, A_{n+1})(1 + R - V(A_n, A_{n+1}))$$

$$J(A_n, A_{n+1}) = \frac{V(A_n, A_{n+1})}{1 + R - V(A_n, A_{n+1})}$$

$$V(A_n, A_{n+1}) = J(A_n, A_{n+1})(1 + R) - J(A_n, A_{n+1}) V(A_n, A_{n+1})$$

$$V(A_n, A_{n+1})(1 + J(A_n, A_{n+1})) = J(A_n, A_{n+1})(1 + R)$$

$$V(A_n, A_{n+1}) = \frac{(1 + R) J(A_n, A_{n+1})}{1 + J(A_n, A_{n+1})}$$

$$V = \frac{\left[1 + \frac{max(\alpha_n, \alpha_{n+1})}{min(\alpha_n, \alpha_{n+1})}\right] J}{1 + J}$$

Supplementary Files

This is a list of supplementary files associated with this preprint. Click to download.

- SupplementaryVideo1Saturatedlogisticmodel.avi
- SupplementaryVideo2Exponentialmodel.avi
- SupplementaryVideo3Calibratedlogisticmodel.avi
- SupplementaryVideo4DiversityKeffratio.avi